Search for new phenomena in dijet events collected in 2015 and 2016 pp collisions with the ATLAS detector at $\sqrt{s} = 13$ TeV

The ATLAS Collaboration

Abstract

This note discusses a search for new physics in events with a pair of jets (dijets) produced in proton-proton collisions in the LHC at a centre-of-mass energy of $\sqrt{s} = 13$ TeV. Mass and angular distributions of dijet events are studied with the ATLAS detector using the data collected in 2015 and 2016, corresponding to an integrated luminosity of 3.5 fb^{-1} and 12.2 fb^{-1}, respectively. No significant deviations from the Standard Model predictions are observed in angular distributions; no significant local excesses are seen in the dijet mass distribution. Exclusion limits are set at 95% CL on a selection of benchmark models and on generic resonant signals. Excited quarks below 5.6 TeV, heavy W bosons below 2.9 TeV, excited W bosons below 3.3 TeV, and quantum black holes with six extra space-time dimensions for quantum gravity scales below 8.7 TeV are excluded. Limits are also set on heavy Z bosons for a range of boson masses and quark couplings in a dark matter mediator model. Non-resonant new physics contributions from contact interaction models are excluded for characteristic scales Λ below 19.9 TeV and 12.6 TeV for constructive and destructive interference with QCD respectively.

1 Introduction

The Large Hadron Collider (LHC) at CERN has been producing proton–proton (pp) collisions at a centre-of-mass energy of $\sqrt{s}$ = 13 TeV since early 2015. With its rapidly increasing statistics and with the increase in parton luminosity at high energy scales between 8 TeV and 13 TeV, this dataset provides a wide scope for searches for new phenomena.

New particles produced in LHC collisions must interact with the constituent partons of the proton. Consequently, the new particles can also produce partons in the final state. Final states including partons often dominate in models of new phenomena beyond the Standard Model (BSM). The partons shower and hadronize, creating collimated jets of particles carrying approximately the four-momenta of the partons. The total production rates for two-jet (dijet) BSM signals can be large, allowing searches for anomalous dijet production to test for such signals even at masses constituting significant fractions of the total hadron collision energy.

In the Standard Model (SM), hadron collisions produce jet pairs primarily via $2 \rightarrow 2$ parton scattering processes governed by quantum chromodynamics (QCD). Far above the confinement scale of QCD ($\approx$ 1 GeV), jets emerge from collisions with large transverse momenta, p_{T}, perpendicular to the direction of the incident partons. For the data analysed here, QCD predicts a smoothly falling dijet invariant mass distribution, m_{jj}. New states decaying to two jets may introduce localised excesses in this distribution. In QCD, due to t-channel poles in the cross-sections for the dominant scattering processes, most dijet production occurs at small angles θ^*, defined as the polar angle in the dijet centre-of-mass frame.[1] Many theories of BSM physics predict additional dijet production with a significant population of jets produced at large angles with respect to the beam; for reviews see Refs. [1, 2]. The search reported in this note exploits these generic features of BSM signals in an analysis of the m_{jj} and dijet angular correlation distributions.

As is common, a rapidity $y = \frac{1}{2} \ln \left(E + p_z \right)/\left(E - p_z \right)$ is defined for each of the outgoing partons, where E is its energy and p_z is the component of its momentum along the beam line.[2] Each incoming parton carries a fraction (Bjorken x) of the momentum of the proton. A momentum imbalance between the two partons boosts the centre-of-mass frame of the collision relative to the laboratory frame along the z direction by $y_{\mathrm{B}} = \frac{1}{2} \ln \left(x_1/x_2 \right) = (y_3 + y_4)/2$, where y_{B} is the rapidity of the boosted centre-of-mass frame, x_1 and x_2 are the fractions of the proton momentum carried by each parton and y_3 and y_4 are the rapidities of the outgoing partons in the detector frame. Differences between two rapidities are invariant under such Lorentz boosts, hence the following function of the rapidity difference $y^* = (y_3 - y_4)/2$ between the two jets,

$$\chi = \mathrm{e}^{2|y^*|} \sim \frac{1 + \cos \theta^*}{1 - \cos \theta^*},$$

---

[1] Since, experimentally, the two partons cannot be distinguished, θ^* is always taken between 0 and $\pi/2$ with respect to the beam.
[2] ATLAS uses a right-handed coordinate system with its origin at the nominal interaction point (IP) in the centre of the detector and the z-axis along the beam line. The x-axis points from the IP to the centre of the LHC ring, and the y-axis points upwards. Cylindrical coordinates (r, ϕ) are used in the transverse plane, ϕ being the azimuthal angle around the z-axis. The pseudorapidity is defined in terms of the polar angle θ as $\eta = -\ln \tan(\theta/2)$. It is equivalent to the rapidity for massless particles.

is the same in the detector frame as in the partonic centre-of-mass frame, defining as θ^* the jet direction with respect to the beam direction in this frame. In the centre-of-mass frame, the two partons have rapidity $\pm y^*$.

The variable χ is constructed such that in the limit of massless parton scattering, and when only t-channel scattering contributes to the partonic cross-section, the angular distribution $\mathrm{d}N/\mathrm{d}\chi$ is approximately independent of χ. The measured shapes of the observed $dN/d\chi$ distributions differ from the parton-level distributions because the observed ones convolve the parton-level distributions with non-uniform parton momentum distributions in x_1 and x_2. Restricting the range of two-parton invariant mass and placing an upper cut on y_B reduces these differences.

Prior investigations of dijet distributions with lower-energy hadron collisions at the S$\bar{\mathrm{p}}$pS [3–5], the Tevatron [6, 7], and the LHC at $\sqrt{s}$ = 7–8 TeV [8–19] did not find BSM phenomena. Recent searches at 13 TeV [20–22] have included extensions of the analysis model to di-b-jet final states [23, 24] and to lower masses [25, 26], but have also observed no significant deviations from the Standard Model. This note presents an analysis of 15.7 fb^{-1} of pp collision LHC data at $\sqrt{s}$ = 13 TeV recorded by the ATLAS detector during 2015 and 2016, focusing on the distributions of m_{jj} and χ with methods based on those used by Ref. [21].

2 ATLAS detector

The ATLAS experiment [27] at the LHC is a multi-purpose particle detector with a forward-backward symmetric cylindrical geometry with layers of tracking, calorimeter, and muon detectors over nearly the entire solid angle around the pp collision point. The directions and energies of high-p_T hadronic jets are measured using silicon tracking detectors and a transition radiation straw-tube tracker, finely segmented hadronic and electromagnetic calorimeters, and a muon spectrometer. A steel/scintillator-tile calorimeter provides hadronic energy measurements for the pseudorapidity range $|\eta| < 1.7$. A lead/liquid-argon (LAr) calorimeter provides electromagnetic (EM) energy measurements with higher granularity within the region $|\eta| < 3.2$. The end-cap and forward regions are instrumented with LAr calorimeters for EM and hadronic energy measurements up to $|\eta| = 4.9$. The lowest-level trigger is implemented in hardware and uses a subset of the detector information to reduce the accepted rate to 100 kHz. This is followed by a software-based high-level trigger that reduces the rate of events recorded to 1 kHz.

3 Event Selection

Collision events are recorded using a trigger requiring the presence of at least one jet reconstructed by the high level trigger with a p_T greater than 380 GeV. Groups of contiguous calorimeter cells (topological clusters) are formed based on the significance of the energy deposit over calorimeter noise [28, 29]. Topological clusters are grouped into jets using the anti-k_t algorithm [30, 31] with radius parameter $R = 0.4$. Jet four-momenta are computed by summing over the topological clusters that constitute each jet, treating the energy of each cluster as a four-momentum with zero mass. Jets with p_T above 20 GeV are reconstructed with an efficiency of 100%. Jet calibrations derived from simulation, and collision data taken at $\sqrt{s}$ = 13 TeV, are used to correct the jet energies and directions to those of the particles from the hard-scatter interaction. This calibration procedure, described in Refs. [32–34], is improved by a data-derived correction to the relative calibration of jets in the central and the forward regions. Analysis

of jet data at 13 TeV using the *in situ* techniques described in Ref. [35] validates the jet calibration and uncertainty estimates. Beyond the p_T range of the *in situ* techniques, for the quantities used to calibrate jets as well as other kinematic quantities, the data agree with simulation within quoted uncertainties. The jet energy scale uncertainty has been evaluated using the 13 TeV data set collected in 2015 and designed for the 2015 and 2016 datasets; the total jet energy scale uncertainty is 1% for central jets with p_T of 500 GeV, and 3% for jets of 2 TeV. The dijet mass resolution is 2.4% and 2%, for dijet masses of 2 and 5 TeV, respectively.

Events containing at least two jets are selected for offline analysis if the p_T of the leading and subleading jets is greater than 440 GeV and 60 GeV, respectively. This requirement ensures a trigger efficiency of at least 99.5% for collisions with $|y^*| < 1.7$ and removes a negligible number of events from unbalanced dijet events originating from additional interactions within the same bunch crossing or jet resolution tails. Events are discarded from the search if any of the three leading jets with $p_T > 60$ GeV is compatible with non-collision background or calorimeter noise [36].

4 Monte Carlo Simulation

For this search, events from QCD processes are simulated with Pythia 8.186 [37] using the A14 [38] set of tuned parameters for the underlying event and the leading-order NNPDF2.3 [39] parton distribution functions (PDFs). The renormalization and factorization scales are set to the average p_T of the two leading jets. Detector effects are simulated using Geant4 [40] within the ATLAS software infrastructure [41]. The same software used to reconstruct data is also used to reconstruct simulated events. The simulated events are used to predict the angular distribution from QCD processes, to test the analytical description of m_{jj} distribution for QCD background, and for qualitative comparisons to kinematic distributions in data. These distributions are also compared to expectations from Pythia 8 Monte Carlo (MC) corrected to next-to-leading-order predictions (NLO) (as discussed below) and found to be in good agreement within experimental uncertainties.

Pythia 8 calculations use matrix elements that are at leading order in the QCD coupling constant with simulation of higher-order contributions partially covered by the parton shower modelling. They also include modelling of hadronisation effects. The distributions of events predicted by Pythia 8 are reweighted to NLO predictions of NLOJET++ [42–44] using mass- and χ-dependent correction factors defined as in Ref. [19]. The correction factors modify the shape of the angular distributions at the level of 15% at low values of χ and high values of m_{jj}. The correction is 5% or less at the highest values of χ. The Pythia 8 predictions also omit electroweak effects. These are included as additional mass- and χ-dependent correction factors [45] that are unity at low m_{jj} and differ from unity by up to 3% in the $m_{jj} > 3.4$ TeV region.

BSM signal samples of excited quarks [46, 47], new heavy vector bosons [48–50], excited chiral bosons [51, 52], quantum black holes (QBH) [53–55] and contact interactions [56–58] are simulated and reconstructed using the same procedure as for QCD processes. The models and the parameters chosen for generation are described in Section 7.
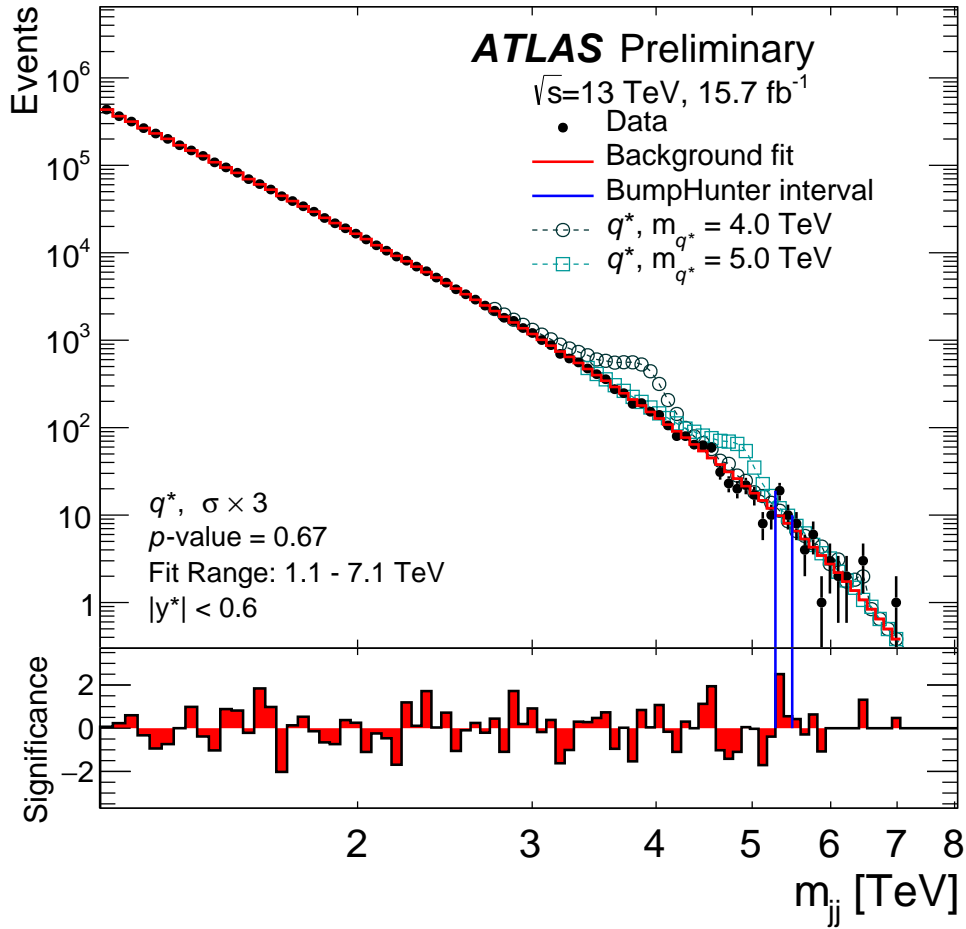
4

Figure 1: The reconstructed dijet mass distribution (filled points) for events with $|y^*| < 0.6$ and $p_T > 440\,(60)$ GeV for the leading (subleading) jets. The solid line depicts the fit to Eq. (1), as discussed in the text. Predictions for an excited quark signal are shown above the fit, normalized to three times the predicted cross-section in order to make the shapes distinguishable above the data. The vertical lines indicate the most discrepant interval identified by the BumpHunter algorithm, for which the p-value is stated in the figure. The lower panel shows the bin-by-bin significances of the data–fit differences, considering only statistical uncertainties.

5 Resonance search

The m_{jj} distribution of events with $|y^*| < 0.6$ is analysed for evidence of contributions from resonant BSM phenomena, where the requirement on $|y^*|$ reduces the background from QCD processes. This nominal ($|y^*| < 0.6$) selection is used for the model independent search phase, to set limits on generic signal shapes, and to constrain the q^*, QBH, W' and Z' benchmark models, all of whose distributions peak at $y^* = 0$. A secondary signal region with a wider cut of $|y^*| < 1.2$ is also defined, optimised for signals produced at more forward angles. The W^* benchmark model whose distribution peaks at $|y^*| > 1.0$ is constrained using this selection. Due to the requirements on y^* and p_T the selection is fully efficient only for $m_{jj} > 1.1$ TeV (1.7 TeV for the $|y^*| < 1.2$ selection). Therefore the analysis is performed above this mass threshold.

Figure 1 shows the observed m_{jj} distribution for events passing the aforementioned nominal resonance

requirements, overlaid with examples of the signals described in Section 7. The bin widths are chosen to approximate the m_{jj} resolution, and therefore widen as the mass increases. The resolution in 13 TeV data was derived from the simulation of QCD processes as in Ref. [21]. The largest value of m_{jj} detected is 7.1 TeV.

To estimate the SM background, the ansatz,

$$f(z) = p_1(1 - z)^{p_2} z^{p_3}, \tag{1}$$

where $z \equiv m_{jj}/\sqrt{s}$, is fit to the m_{jj} distribution in Fig. 1 to obtain the parameters p_i. The fit range is 1.1–7.1 TeV. CDF, CMS, and ATLAS dijet searches such as those described in Refs. [6, 8, 13, 14, 17] have found that expressions similar to Eq. (1) describe dijet mass distributions observed at lower collision energies. The ansatz also describes leading-order and NLO simulations of QCD dijet production at $\sqrt{s} = 13$ TeV. A log-likelihood-ratio statistic employing Wilks' theorem [59] is used to determine if the background estimation would be significantly improved by an additional degree of freedom. With the current dataset, Eq. (1) is found to be sufficient.

Figure 1 also shows the result of the fit. The lower panel of the figure shows the significances of bin-by-bin differences between the data and the fit following the convention described in Ref. [60]. These Gaussian significances are calculated from the Poisson probability, considering only statistical uncertainties.

The uncertainty in values of the parameters in Eq. (1) is evaluated by fitting them to pseudo-data drawn via Poisson fluctuations around the fitted background model. The uncertainty in the prediction in each m_{jj} bin is taken to be the root mean square of the function value for all pseudo-experiments in that bin. To estimate an uncertainty due to the choice of the background parameterization, a parameterization with one additional parameter, $f(z) \cdot z^{p_4 \log z}$, is compared to the nominal ansatz, and the difference is taken as an uncertainty. The prediction of the m_{jj} distribution does not involve simulated collisions and thus the fit is not affected by theoretical or experimental uncertainties.

The statistical significance of any localized excess in the m_{jj} distribution is quantified using the BumpHunter algorithm [61, 62]. The algorithm compares the binned m_{jj} distribution of the data to the fitted background estimate, considering contiguous mass intervals in all possible locations, from a width of two bins to a width of half of the distribution. For each interval in the scan, it computes the significance of any excess found. The algorithm identifies the interval 5277–5487 GeV, indicated by the two vertical lines in Fig. 1, as the most discrepant interval. The statistical significance of this outcome is evaluated using the ensemble of possible outcomes across all intervals scanned, by applying the algorithm to many pseudo-data samples drawn randomly from the background fit. Without including systematic uncertainties, the probability that fluctuations of the background model would produce an excess at least as significant as the one observed in the data, anywhere in the distribution, is 0.67. Thus, there is no evidence of a localized contribution to the mass distribution from BSM phenomena. The search in the secondary signal region similarly shows no deviation from the smooth background parameterisation, and gives a BumpHunter probability of 0.83.

6 Angular search

The $dN/d\chi$ (angular) distributions of events with $|y^*| < 1.7$ (i.e. $\chi < 30.0$) and $|y_B| < 1.1$ are also analysed for contributions from BSM signals. The data with $m_{jj} < 2.5$ TeV are discarded to remove bias from the kinematic selections described earlier.

Figure 2 shows the angular distributions of the data in different m_{jj} ranges, the SM prediction for the shape of the angular distributions, and examples of the signals described in Section 7. The highest m_{jj} measured is 7.9 TeV. The SM prediction is obtained from simulation, as described in Section 4, including the aforementioned corrections. In the data analysis, the prediction from simulation in each m_{jj} range is normalized to match the integral of the data in the same range.

Theoretical uncertainties in simulations of the angular distributions from QCD processes are estimated as described in Ref. [21]. The effect on the QCD prediction of varying the PDFs is estimated using NLOJET++ with three different PDF sets: CT10 [63], MSTW2008 [64] and NNPDF23 [39]. As the choice of PDF mainly affects the total cross-section rather than the shape of the χ distributions, these uncertainties are negligible ($< 1\%$) in this analysis. The uncertainty due to the choice of renormalization and factorization scales is estimated using NLOJET++ by varying each one independently up and down by a factor two, excluding opposite variations. The resulting uncertainty, taken as the envelope of the variations in the normalized χ distributions, depends on both m_{jj} and χ, rising to 30% at the smallest χ values at high m_{jj} values. The statistical uncertainty of the simulated NLO corrections is less than 1%. The dominant experimental uncertainty in the predictions of the χ distributions is the jet energy scale uncertainty, with an impact of at most 15% at high m_{jj} values. The uncertainty in the jet energy resolution has negligible impact. The theoretical uncertainties and the total uncertainties are displayed as shaded bands around the prediction.

The CL_s technique [65, 66] is used to test the compatibility of the χ distribution with the SM prediction and with the BSM signals discussed in Section 7, using a combined fit in four coarse m_{jj} bins covering $m_{jj} > 3.4$ TeV. No significant deviation of the data from the background-only hypothesis is observed, with a CL_b of 0.07.

7 Benchmark signals

The data are used to constrain several of the many BSM models that predict dijet excesses. Quantum black holes, excited quarks, and W', W^*, and Z' bosons would produce peaks in the m_{jj} distribution. Contact interactions would introduce smooth changes in the high-mass tail of the m_{jj} distribution that could be detected in the analysis of the χ distributions. The signal models are simulated using the parton-level generators indicated below, in an identical manner to QCD processes, using the same PDFs and parameters for non-perturbative effects, except where noted otherwise.

The LHC could produce black holes with masses at or above the fundamental scale of gravity, M_D, if that scale is lowered to a few TeV by the existence of extra spatial dimensions [2, 53, 54, 67–70]. High-multiplicity final states from thermalizing black holes are explored at $\sqrt{s} = 13$ TeV by ATLAS in Refs. [71, 72]. This analysis explores QBH, which would be produced near M_D and decay into a few particles rather than high-multiplicity final states [53–55, 73], appearing in the m_{jj} distribution as an excess localized at the threshold mass for the quantum black hole production, M_{th}. Here, production and decay to two jets is simulated using the BLACKMAX (BM) generator [55] assuming an Arkani-Hamed–Dimopoulous–Dvali (ADD) scenario [74, 75] with $M_D = M_{th}$ and a number of extra dimensions $n = 6$, as in Ref. [17]. In these models, the branching ratio to dijets is greater than 96%. The acceptance times efficiency of the resonance selection for quantum black holes is approximately 53% across all studied masses. The PDFs used are CTEQ6L1 [76]. The QBH signals peak slightly above their threshold values and have negligible low-mass tails. The reconstructed signal peaks have width-to-mass ratios in their central regions of approximately 10%.
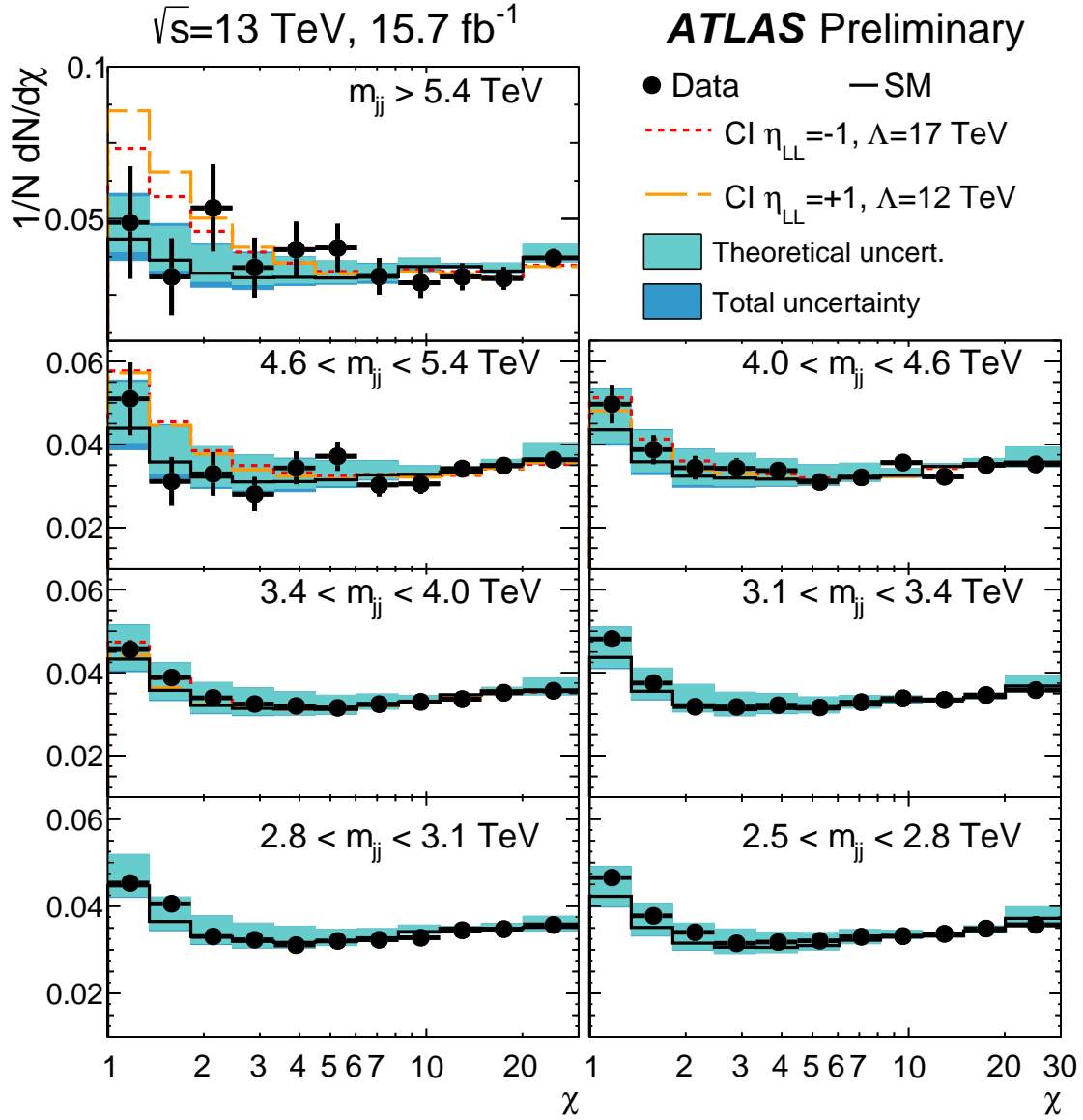
Figure 2: Reconstructed distributions of the dijet angular variable χ in different regions of the dijet invariant mass m_{jj} for events with $|y^*| < 1.7$, $|y_B| < 1.1$ and $p_T > 440$ (60) GeV for the leading (subleading) jets. Shown are the data (points), PYTHIA predictions with NLO QCD and EW corrections applied (solid lines), and examples of the contact interaction (CI) signals discussed in the text (dashed lines). The theoretical uncertainties and the total theoretical and experimental uncertainties on the predictions are displayed as shaded bands around the SM prediction.

Excited quarks (q^*) [46, 47] are predicted in models of compositeness and are a benchmark for quark–gluon resonances [8, 9, 14, 15]. The q^* model is simulated with PYTHIA 8, assuming spin-1/2 excited quarks with coupling constants the same as for SM quarks. The renormalization and factorization scales are set to the average p_T of the two leading jets. Only the decay of the excited quark to a gluon and an up- or down-type quark is simulated; this corresponds to a branching ratio of 85%. Before parton shower effects are taken into account, the intrinsic width of the q^* signals is comparable to the detector resolution.

After showering, a radiative tail is present which increases in strength for q^*s of higher masses. The resonance selection acceptance times efficiency for a q^* with a mass of 4 TeV is 58%.

Additional spin-1 W' and Z' bosons often arise in the symmetry breaking of extended gauge theories. A W' model [48] with $V–A$ SM couplings and a corresponding branching ratio to dijets of 75% is considered. In this analysis, events are simulated in PYTHIA 8 and decays are restricted to quark–antiquark pairs with all six quark flavours included. Events including top decays are not removed from the analysis. A leptophobic Z' model [49] is also simulated, with matrix elements calculated in MADGRAPH 5 [77] and parton showering performed in PYTHIA 8. The Z' model assumes axial-vector couplings to all SM quarks and to a Dirac fermion dark matter candidate. Final states with top quarks are not simulated, and no interference with the SM is simulated for either the W' or the Z' model. The Z' model considered follows a scenario [50] where its decays to dark matter is negligible, hence the dijet production rate and resonance width depend only on the coupling to quarks, g_q, and the mass of the resonance $m_{Z'}$. Before parton shower effects are considered, the intrinsic width of the Z' signal ranges from 0.05% for a Z' with a mass of 1.5 TeV and $g_q = 0.1$ to 10% for a Z' with a mass of 3.5 TeV and $g_q = 0.5$. The W' signal has a similar intrinsic width to a Z' of coupling $g_q = 0.3$ at every mass point considered. For $g_q > 0.5$ the intrinsic width of the Z' resonance is greater than 15%, resulting in a very wide peak and in a loss of sensitivity of the resonant search, which is therefore limited to $g_q \leq 0.5$. The resonance selection acceptance times efficiency for a mass of 3 TeV is 40% for the W' model and 47% for the Z' model with $g_q = 0.2$. Because of the large radiative tails of the W' signals, the acceptance for this model increases to a maximum at approximately 2.5 TeV and then decreases again to $< 20\%$ for masses above 6.0 TeV.

A new excited W^* boson [51, 52] is generated through a simplified model [78] in the CalcHEP 3.6 generator, in combination with the NNPDF23 NLO PDF set and PYTHIA 8 for the simulation of non-perturbative effects. The sine of the mixing angle in this model ($\sin\theta_X$) is set to zero, producing leptophobic decays of the W^* that are limited to all SM quarks. The angular distribution of the W^* differs from that of the other signals under study, peaking at y^* values above 1. As a result this benchmark model is constrained using the alternate signal region with $|y^*| < 1.2$. The acceptance for the leptophobic W^* signal with this selection increases from 33% around 2 TeV to nearly 60% for the highest masses examined.

Results are also provided as limits on the cross-section times acceptance times branching ratio to two jets, $\sigma \times A \times \mathrm{BR}$, of a hypothetical signal that produces a Gaussian contribution to the observed m_{jj} distribution. For sufficiently narrow resonances, these results may be used to set limits in BSM models beyond those considered explicitly in this note. These limits should be used when PDF and non-perturbative effects are not dominant and, after applying the resonance selection, the reconstructed m_{jj} distribution predicted by the model approaches a Gaussian distribution. Predicted BSM signals with an intrinsic width much smaller than 5% should be compared to the limit curve for width equal to the experimental resolution. Predicted signals with larger widths should be compared with the limit that corresponds most closely to the width of the Gaussian contribution predicted by the model. More details can be found in Appendix A of Ref. [17].

For all signals described above, the following systematic uncertainties are included in the limit setting: jet energy scale, PDF acceptance uncertainty, and luminosity. The jet energy uncertainty ranges from 1.5% at the lowest masses to 3% for masses above 4.5 TeV. On average, the PDF uncertainty affects the angular distributions by 1%. The preliminary uncertainty on the combined 2015+2016 integrated luminosity is 2.9%. It is derived, following a methodology similar to that detailed in Refs. [79] and [80], from a preliminary calibration of the luminosity scale using x-y beam-separation scans performed in August 2015 and May 2016.

The dijet distributions can also be modified by new mediating particles with a mass much higher than that which can be probed directly. A four-fermion effective field theory (contact interaction) [56–58] characterized by a single energy scale Λ can be used to describe these effects:

$$L_{qq} = \frac{2\pi}{\Lambda^2}[\quad \eta_{LL}(\bar{q}_L\gamma^\mu q_L)(\bar{q}_L\gamma_\mu q_L)$$
$$+\eta_{RR}(\bar{q}_R\gamma^\mu q_R)(\bar{q}_R\gamma_\mu q_R)$$
$$+2\eta_{RL}(\bar{q}_R\gamma^\mu q_R)(\bar{q}_L\gamma_\mu q_L)], \qquad (2)$$

where the quark fields have L and R chiral projections and the coefficients η_{LL}, η_{RR}, and η_{RL} activate various interactions. Contact interactions with a non-zero left-chiral colour-singlet coupling ($\eta_{LL} = \pm1$, $\eta_{RL} = \eta_{RR} = 0$) are simulated using PYTHIA 8. This type of coupling is chosen because its angular distributions are representative of those of other BSM models. Interference of the signal model with the SM process $q\bar{q} \rightarrow q\bar{q}$ is included. Events are simulated for both constructive and destructive interference with $\Lambda = 7$ TeV. From this sample, the angular distributions for other values of Λ are obtained using the fact that the interference term is proportional to $1/\Lambda^2$ and the pure contact-interaction cross-section is proportional to $1/\Lambda^4$. The PYTHIA 8 signal prediction is reweighted to the NLO cross-sections provided by CIJET [81]. Uncertainties in the prediction of the angular distributions for contact-interaction signals are obtained in the same manner as for QCD processes.

8 Results

Starting from the m_{jj} distribution obtained with the resonance selection, a Bayesian method [14] is applied to the data and simulation of signals at a series of discrete masses to set 95% credibility-level (CL) upper limits on the cross-section times acceptance for the signals described above. The method uses a constant prior for signal cross-section and Gaussian priors for nuisance parameters corresponding to systematic uncertainties. The expected limits are calculated using pseudo-experiments generated from the maximum-likelihood values for parameters of the background-only model in Eq. (1) using the full systematic uncertainties in both the signal and background models. The limit is interpolated logarithmically between the discrete masses to create curves continuous in signal mass. The mass limits for each of those models are shown in Figs. 3 and 4 and Table 1. No uncertainty on the theoretical cross-section for the signals is assessed.

Figure 5 shows limits on the Gaussian contributions to the observed m_{jj} distribution obtained for a mean mass m_G and four different widths, from a width equal to the detector mass resolution [21] to a width of 15% of the mean of the Gaussian mass distribution. Limits are set only when m_G is within 1.1–7.1 TeV and separated by at least the width of the Gaussian from the endpoints of this range. Intrinsically narrow resonances with effective cross-sections exceeding values ranging from approximately 10–100 fb for masses below 2 TeV to 1–3 fb for masses above 5 TeV are excluded. As the width increases, the expected signal contribution is distributed across more bins. Therefore wider signals are affected less than narrower signals by statistical fluctuations of the data in a single bin.

Starting from the χ distribution obtained with the angular selection, the CL_s method is used to set limits on signal contributions from contact interactions, using the background predicted by the SM simulations as the null hypothesis. The asymptotic approximation [82] of a profile likelihood ratio is used to set 95% confidence-level limits. A combined fit is performed on the four highest-m_{jj} regions of Fig. 2. The correlation of the systematic uncertainties between the regions is taken into account and allows the
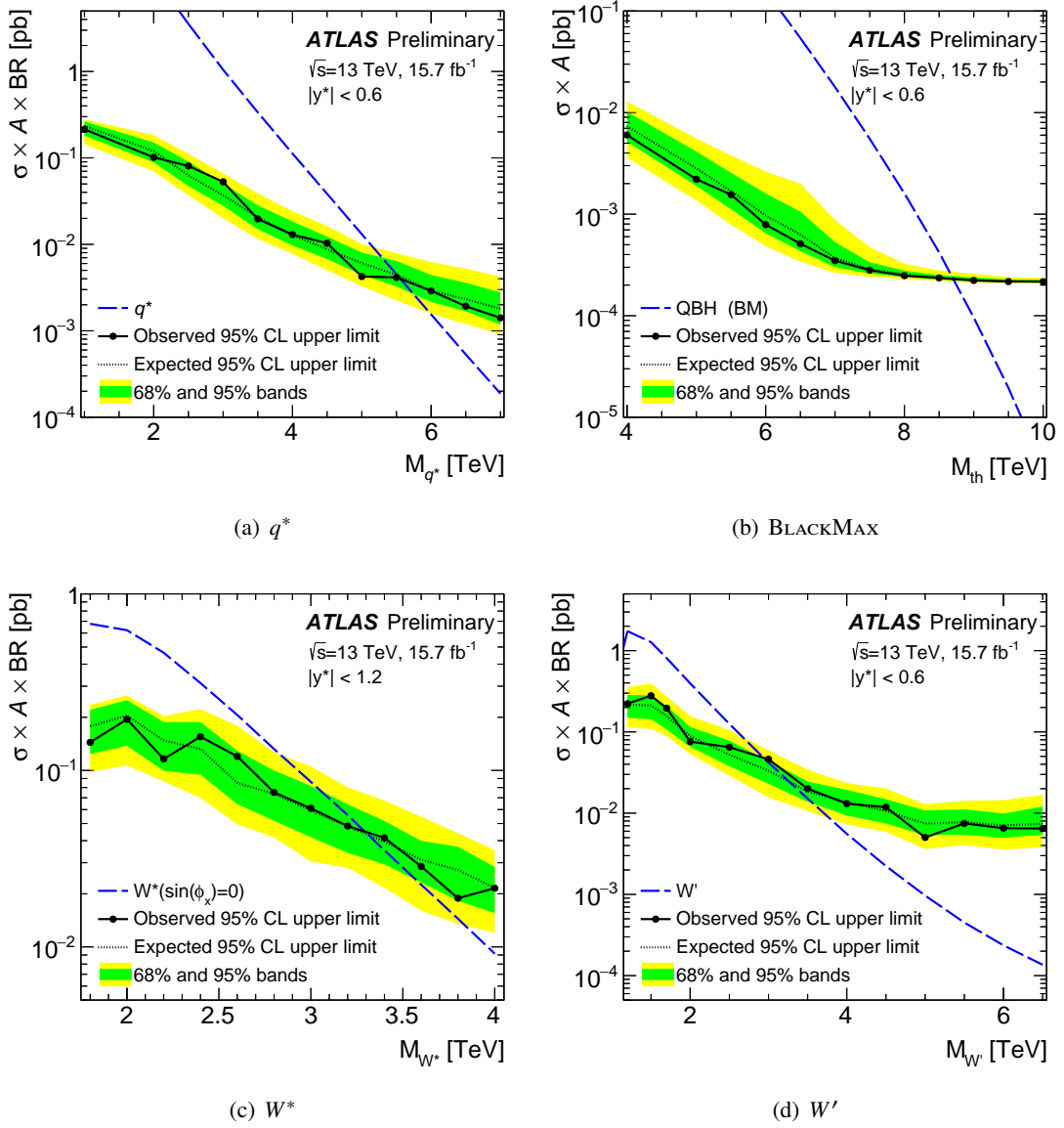
(a) q^*

(b) BLACKMAX

(c) W^*

(d) W'

Figure 3: The 95% credibility-level upper limits obtained from the m_{jj} distribution on cross-section, σ, times acceptance, A, for the models described in the text. Clockwise from top left: q^*, quantum black holes with $n = 6$ generated with BLACKMAX, W' and W^* where the first three use the nominal selection and the last uses the widened $|y^*| < 1.2$ selection. The numerical values of the observed and expected limits are summarised in Table 1.

constraint of the largest uncertainties by the lowest m_{jj} regions considered. The maximum likelihood values of the nuisance parameters do not differ significantly from the expectations. The bounds on contact interactions thus obtained are shown in Fig. 6 and in Table 1.

Model	95% CL exclusion limit	
	Observed	Expected
Quantum black holes, ADD (BLACKMAX generator)	8.7 TeV	8.7 TeV
Excited quark	5.6 TeV	5.5 TeV
W'	2.9 TeV	3.3 TeV
W^*	3.3 TeV	3.3 TeV
Contact interactions (η_{LL} =+1)	12.6 TeV	13.7 TeV
Contact interactions (η_{LL} =-1)	19.9 TeV	23.7 TeV

Table 1: The 95% credibility-level lower limit on the mass of quantum black holes, W' and W^* models, and excited quarks from the resonance selection, and the 95% confidence-level lower limit on the scale of contact interactions for constructive ($\eta_{LL} = -1$) and destructive ($\eta_{LL} = +1$) from the angular selection. Limits on the Z' model are provided in Fig. 4.
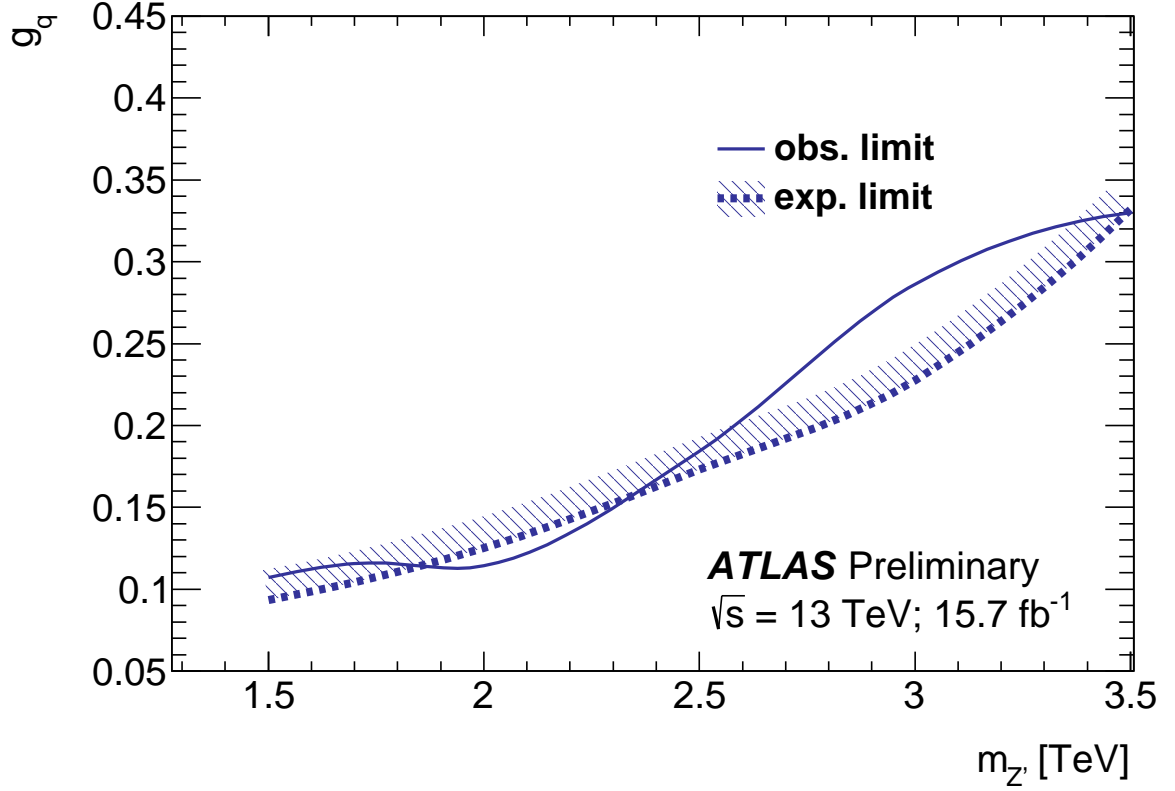
Figure 4: The ratio of 95% credibility-level upper limits to predicted cross-sections with respect to the Z' model predictions described in the text, as a function of the coupling to quarks, g_q, and the mass, $M_{Z'}$, obtained from the m_{jj} distribution. Mass points were simulated with 0.5 TeV spacing and additionally at 1.7 TeV. For $g_q > 0.5$ the Z' resonance is no longer narrow (its intrinsic width becomes greater than 15%).
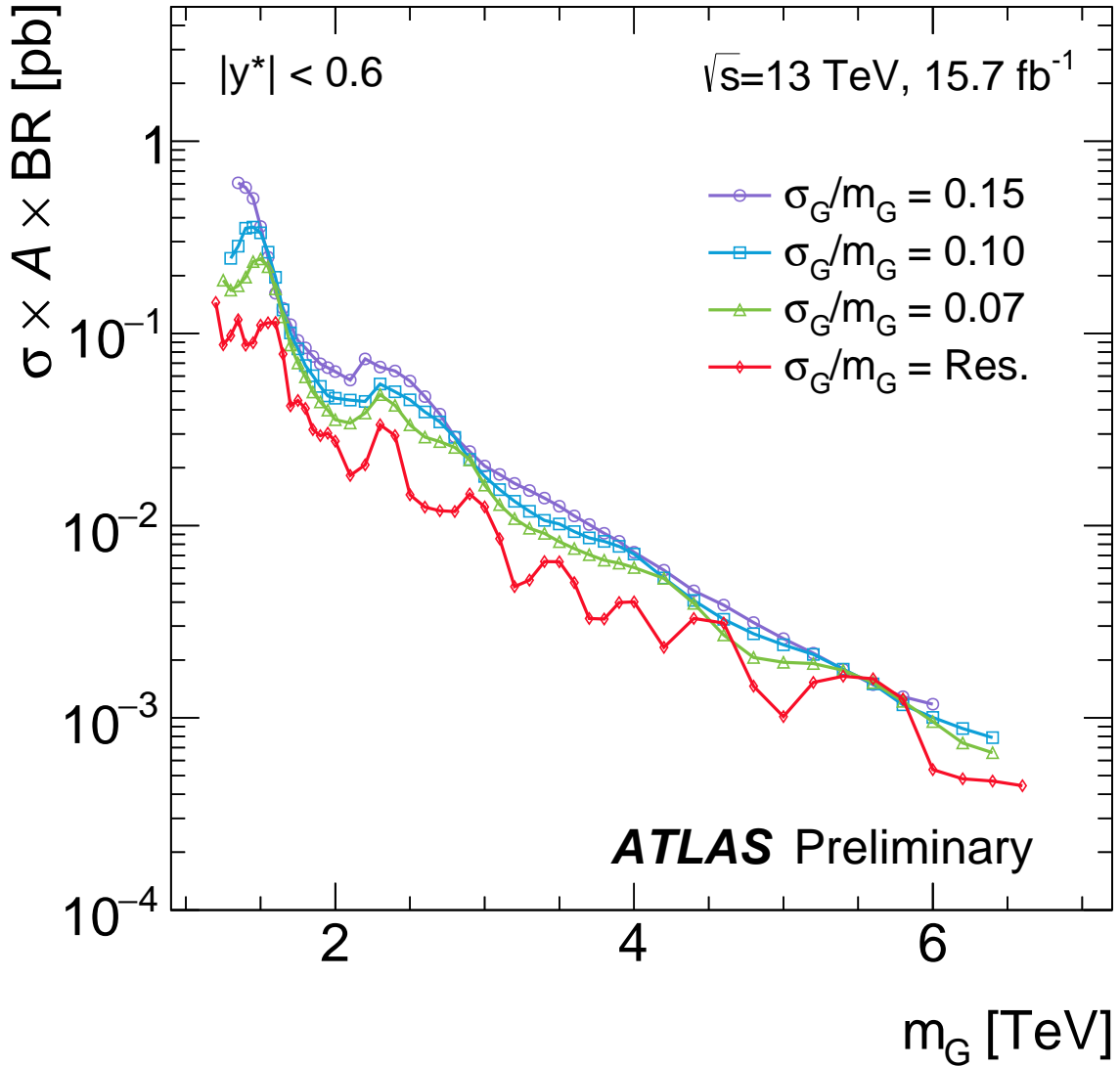
Figure 5: The 95% credibility-level upper limits obtained from the m_{jj} distribution on cross-section times acceptance times branching ratio to two jets, $\sigma \times A \times BR$, for a hypothetical signal with a cross-section σ_G that produces a Gaussian contribution to the observed m_{jj} distribution, as a function of the mean mass of the Gaussian distribution, m_G. Limits are obtained for four different widths, from a width equal to the detector mass resolution ("Res."), 3%–2% depending on m_{jj} probed, to 15% of the mean of the Gaussian mass distribution.

9 Conclusion

No evidence of phenomena beyond the Standard Model is uncovered in this search using dijet events in 15.7 fb^{-1} of proton–proton collisions with a centre-of-mass energy of $\sqrt{s} = 13$ TeV recorded by the ATLAS detector at the Large Hadron Collider. The dijet invariant mass distribution exhibits no significant local excesses above a data-derived estimate of the smoothly falling distribution predicted by the Standard Model. The dijet angular distributions also agree with a Monte Carlo simulation of the SM. With the
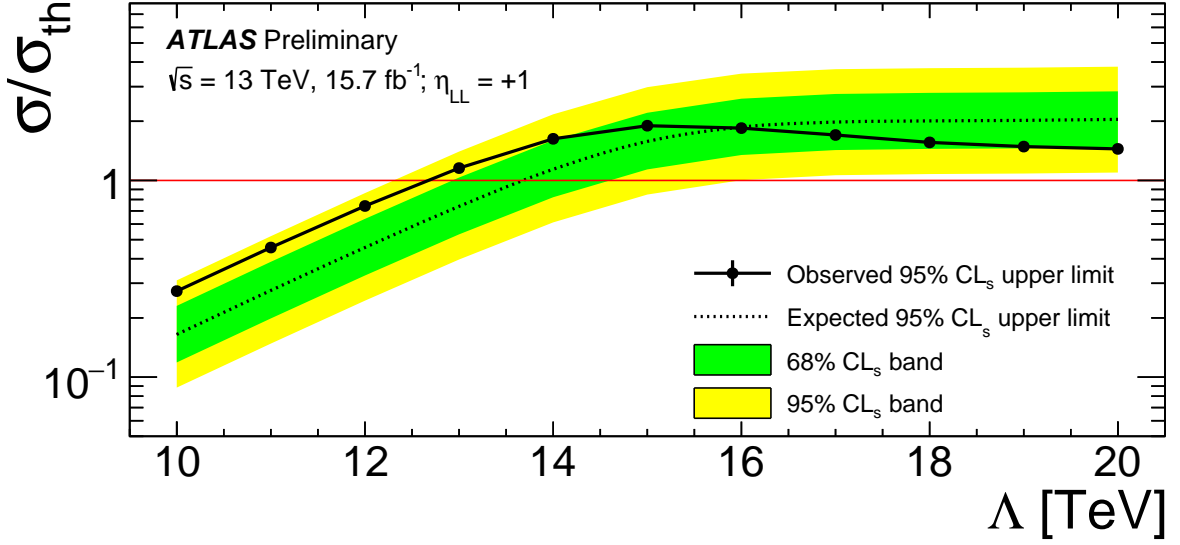
(a)
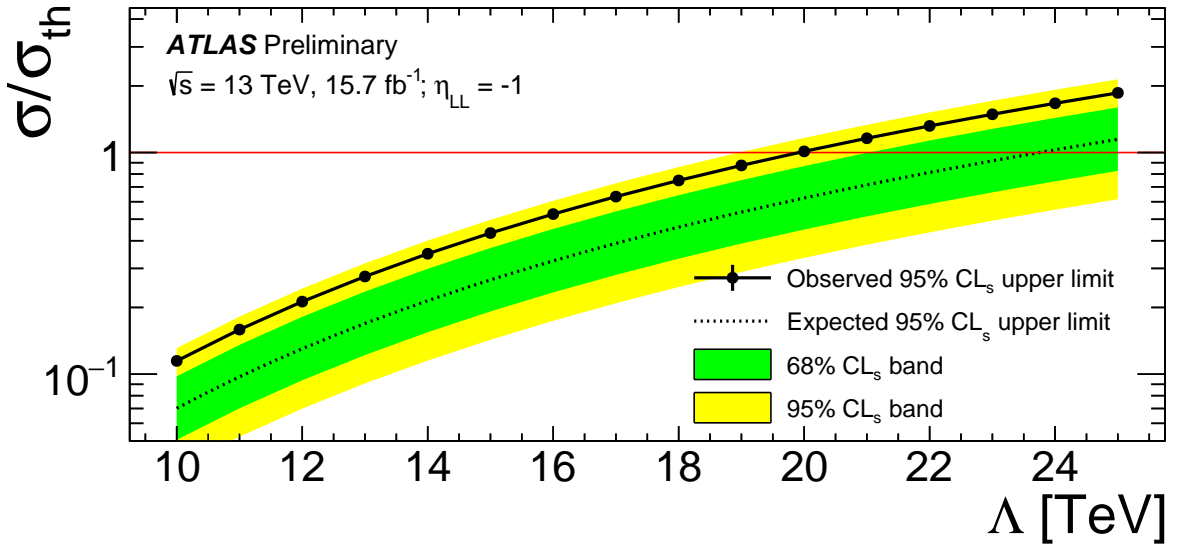
(b)

Figure 6: Ratio of the observed and expected 95% confidence-level upper limits on the cross-section in the contact interaction model to the predicted cross-section σ/σ_{th} as a function of compositeness scale Λ, for (top) destructive and (bottom) constructive interference with QCD processes. The crossing of the observed and expected 95% confidence-level lines with the line at signal strength of one indicates observed and expected lower limits on Λ, respectively.

resonance selection, the analysis excludes at 95% credibility level several types of signals, as predicted by models of quantum black holes, excited quarks, W', W^* and Z' bosons. It also sets 95% credibility-level upper limits on the cross-section for new processes that would produce a Gaussian contribution to the dijet mass distribution. It excludes Gaussian contributions if the effective cross-section exceeds values ranging

from approximately 10–100 fb for masses below 2 TeV to 1–3 fb for masses above 5 TeV. With the angular selection, 95% confidence-level lower limits are set on the compositeness scale of contact interactions at 12.6 TeV (19.9 TeV) for destructive (constructive) interference between the new interaction and QCD processes. These results extend the exclusions obtained using the 2015 dataset by up to 15% in mass.

References

[1] R. M. Harris and K. Kousouris, *Searches for dijet resonances at hadron colliders*, Int. J. Mod. Phys. A **26** (2011) 5005, arXiv: 1110.5302 [hep-ex].

[2] N. Boelaert and T. Åkesson, *Dijet angular distributions at $\sqrt{s}$ = 14 TeV*, Eur. Phys. J. C **66** (2010) 343, arXiv: 0905.3961 [hep-ph].

[3] UA1 Collaboration, G. Arnison et al., *Angular distributions and structure functions from two jet events at the CERN SPS p anti-p collider*, Phys. Lett. B **136** (1984) 294.

[4] UA1 Collaboration, C. Albajar et al., *Two jet mass distributions at the CERN Proton–Anti-Proton Collider*, Phys. Lett. B **209** (1988) 127.

[5] UA2 Collaboration, P. Bagnaia et al., *Measurement of jet production properties at the CERN pp Collider*, Phys. Lett. B **144** (1984) 283.

[6] CDF Collaboration, T. Aaltonen et al., *Search for new particles decaying into dijets in proton-antiproton collisions at $\sqrt{s}$ = 1.96 TeV*, Phys. Rev. D **79** (2009) 112002, arXiv: 0812.4036 [hep-ex].

[7] D0 Collaboration, V. M. Abazov et al., *Measurement of dijet angular distributions at $\sqrt{s}$ = 1.96 TeV and searches for quark compositeness and extra spatial dimensions*, Phys. Rev. Lett. **103** (2009) 191803, arXiv: 0906.4819 [hep-ex].

[8] ATLAS Collaboration, *Search for New Particles in Two-Jet Final States in 7 TeV Proton–Proton Collisions with the ATLAS Detector at the LHC*, Phys. Rev. Lett. **105** (2010) 161801, arXiv: 1008.2461 [hep-ex].

[9] ATLAS Collaboration, *Search for quark contact interactions in dijet angular distributions in pp collisions at $\sqrt{s}$ = 7 TeV measured with the ATLAS detector*, Phys. Lett. B **694** (2011) 327, arXiv: 1009.5069 [hep-ex].

[10] CMS Collaboration, *Search for Dijet Resonances in 7 TeV pp Collisions at CMS*, Phys. Rev. Lett. **105** (2010) 211801, arXiv: 1010.0203 [hep-ex].

[11] CMS Collaboration, *Search for Quark Compositeness with the Dijet Centrality Ratio in pp Collisions at $\sqrt{s}$ = 7 TeV*, Phys. Rev. Lett. **105** (2010) 262001, arXiv: 1010.4439 [hep-ex].

[12] CMS Collaboration, *Measurement of Dijet Angular Distributions and Search for Quark Compositeness in pp Collisions at $\sqrt{s}$ = 7 TeV*, Phys. Rev. Lett. **106** (2011) 201804, arXiv: 1102.2020 [hep-ex].

[13] CMS Collaboration, *Search for Resonances in the Dijet Mass Spectrum from 7 TeV pp Collisions at CMS*, Phys. Lett. B **704** (2011) 123, arXiv: 1107.4771 [hep-ex].

[14] ATLAS Collaboration, *A search for new physics in dijet mass and angular distributions in pp collisions at $\sqrt{s}$ = 7 TeV measured with the ATLAS detector*, New J. Phys. **13** (2011) 053044, arXiv: 1103.3864 [hep-ex].

[15] ATLAS Collaboration, *Search for new physics in the dijet mass distribution using 1 fb^{-1} of pp collision data at $\sqrt{s}$ = 7 TeV collected by the ATLAS detector*, Phys. Lett. B **708** (2012) 37, arXiv: 1108.6311 [hep-ex].

[16] ATLAS Collaboration, *ATLAS search for new phenomena in dijet mass and angular distributions using pp collisions at $\sqrt{s}$ = 7 TeV*, JHEP **01** (2013) 029, arXiv: 1210.1718 [hep-ex].

[17] ATLAS Collaboration, *Search for new phenomena in the dijet mass distribution using pp collision data at $\sqrt{s}$ = 8 TeV with the ATLAS detector*, Phys. Rev. D **91** (2015) 052007, arXiv: 1407.1376 [hep-ex].

[18] CMS Collaboration, *Search for narrow resonances using the dijet mass spectrum in pp collisions at $\sqrt{s}$ = 8 TeV*, Phys. Rev. D **87** (2013) 114015, arXiv: 1302.4794 [hep-ex].

[19] ATLAS Collaboration, *Search for New Phenomena in Dijet Angular Distributions in Proton–Proton Collisions at $\sqrt{s}$ = 8 TeV Measured with the ATLAS Detector*, Phys. Rev. Lett. **114** (2015) 221802, arXiv: 1504.00357 [hep-ex].

[20] CMS Collaboration, *Search for narrow resonances decaying to dijets in proton–proton collisions at $\sqrt{s}$ = 13 TeV*, Phys. Rev. Lett. **116** (2016) 071801, arXiv: 1512.01224 [hep-ex].

[21] ATLAS Collaboration, *Search for New Phenomena in Dijet Mass and Angular Distributions from pp Collisions at $\sqrt{s}$ = 13 TeV with the ATLAS Detector*, Phys. Lett. B **754** (2016) 302, arXiv: 1512.01530 [hep-ex].

[22] CMS Collaboration, *Searches for quark contact interactions and extra spatial dimensions with dijet angular distributions in proton proton collisions at 13 TeV*, CMS-PAS-EXO-15-009 (2015), URL: https://cds.cern.ch/record/2114812?ln=en.

[23] ATLAS Collaboration, *Search for new physics using events with b-jets and a pair of same charge leptons in 3.2 fb^{-1} of pp collisions at $\sqrt{s}$ = 13 TeV with the ATLAS detector*, ATLAS-CONF-2016-032 (2016), URL: https://cds.cern.ch/record/2161545.

[24] ATLAS Collaboration, *Search for resonances below 1.2 TeV from the mass distribution of b-jet pairs in proton-proton collisions at $\sqrt{s}$=13 TeV with the ATLAS detector*, ATLAS-CONF-2016-031 (2016), URL: https://cds.cern.ch/record/2161136.

[25] ATLAS Collaboration, *Search for light dijet resonances with the ATLAS detector using a Trigger-Level Analysis in LHC pp collisions at $\sqrt{s}$ = 13 TeV*, ATLAS-CONF-2016-030 (2016), URL: https://cds.cern.ch/record/2161135.

[26] ATLAS Collaboration, *Search for new light resonances decaying to jet pairs and produced in association with a photon in proton-proton collisions at $\sqrt{s}$ = 13 TeV with the ATLAS detector*, ATLAS-CONF-2016-029 (2016), URL: https://cds.cern.ch/record/2161134.

[27] ATLAS Collaboration, *The ATLAS Experiment at the CERN Large Hadron Collider*, JINST **3** (2008) S08003.

[28] W. Lampl et al., *Calorimeter clustering algorithms: description and performance*, ATL-LARG-PUB-2008-002, 2008, URL: http://cds.cern.ch/record/1099735.

[29] ATLAS Collaboration, *Topological cell clustering in the ATLAS calorimeters and its performance in LHC Run 1*, (2016), arXiv: 1603.02934 [hep-ex].

[30] M. Cacciari, G. Salam and G. Soyez, *The anti-k_T jet clustering algorithm*, JHEP **04** (2008) 063, arXiv: 0802.1189 [hep-ph].

[31] M. Cacciari and G. P. Salam, *Dispelling the N^3 myth for the k_t jet-finder*, Phys. Lett. B **641** (2006) 57, arXiv: hep-ph/0512210.

[32] ATLAS Collaboration, *Performance of pile-up mitigation techniques for jets in pp collisions with the ATLAS detector*, Nucl. Instrum. Meth. A **824** (2016) 367, arXiv: 1510.03823 [hep-ex].

[33] ATLAS Collaboration, *Data-driven determination of the energy scale and resolution of jets reconstructed in the ATLAS calorimeters using dijet and multijet events at $\sqrt{s}$ = 8 TeV*, ATLAS-CONF-2015-017, 2015, URL: http://cdsweb.cern.ch/record/2008678.

[34] ATLAS Collaboration, *Jet calibration and systematic uncertainties for jets reconstructed in the ATLAS detector at $\sqrt{s}$ = 13 TeV*, ATL-PHYS-PUB-2015-015, 2015, URL: http://cds.cern.ch/record/2037613.

[35] ATLAS Collaboration, *Jet global sequential corrections with the ATLAS detector in proton–proton collisions at $\sqrt{s}$ = 8 TeV*, ATLAS-CONF-2015-002, 2015, URL: http://cdsweb.cern.ch/record/2001682.

[36] ATLAS Collaboration, *Selection of jets produced in* 13 *TeV proton–proton collisions with the ATLAS detector*, ATLAS-CONF-2015-029, 2015, URL: http://cdsweb.cern.ch/record/2037702.

[37] T. Sjostrand, S. Mrenna and P. Skands, *A brief introduction to Pythia 8.1*, Comput. Phys. Commun. **178** (2008) 852, arXiv: 0710.3820 [hep-ph].

[38] ATLAS Collaboration, *ATLAS Run 1 Pythia 8 tunes*, ATLAS-PHYS-PUB-2014-021 (2014), URL: http://cds.cern.ch/record/1966419.

[39] R. D. Ball et al., *Parton distributions with LHC data*, Nucl. Phys. B **867** (2013) 244, arXiv: 1207.1303 [hep-ph].

[40] S. Agostinelli et al., *GEANT4: a simulation toolkit*, Nucl. Instrum. Meth. A **506** (2003) 250.

[41] ATLAS Collaboration, *The ATLAS simulation infrastructure*, Eur. Phys. J. C **70** (2010) 823, arXiv: 1005.4568 [physics.ins-det].

[42] Z. Nagy, *Three-jet cross sections in hadron-hadron collisions at next-to-leading-order*, Phys. Rev. Lett. **88** (2002) 122003, arXiv: hep-ph/0110315 [hep-ph].

[43] Z. Nagy, *Next-to-leading order calculation of three-jet observables in hadron-hadron collision*, Phys. Rev. D **68** (2003) 094002, arXiv: hep-ph/0307268 [hep-ph].

[44] S. Catani and M. H. Seymour, *A general algorithm for calculating jet cross-sections in NLO QCD*, Nucl. Phys. B **485** (1997) 291, arXiv: hep-ph/9605323 [hep-ph].

[45] S. Dittmaier, A. Huss and C. Speckner, *Weak radiative corrections to dijet production at hadron colliders*, JHEP **11** (2012) 095, arXiv: 1210.0438 [hep-ph].

[46] U. Baur, I. Hinchliffe and D. Zeppenfeld, *Excited quark production at hadron colliders*, Int. J. Mod. Phys. A **2** (1987) 1285.

[47] U. Baur, M. Spira and P. M. Zerwas, *Excited quark and lepton production at hadron colliders*, Phys. Rev. D **42** (1990) 815.

[48] G. Altarelli, B. Mele and M. Ruiz-Altaba, *Searching for new heavy vector bosons in $p\bar{p}$ colliders*, Z. Phys. C **45** (1989) 109, [Erratum: Z. Phys. C 47, 676(1990)].

[49] D. Abercrombie et al., *Dark matter benchmark models for early LHC Run-2 searches: report of the ATLAS/CMS Dark Matter Forum*, 2015, arXiv: `1507.00966 [hep-ex]`.

[50] M. Chala et al., *Constraining dark sectors with monojets and dijets*, JHEP **07** (2015) 089, arXiv: `1503.05916 [hep-ph]`.

[51] M. V. Chizhov, V. A. Bednyakov and J. A. Budagov, *A unique signal of excited bosons in dijet data from pp-collisions*, Phys. Atom. Nucl. **75** (2012) 90, arXiv: `1010.2648 [hep-ph]`.

[52] M. V. Chizhov and G. Dvali, *Origin and Phenomenology of Weak-Doublet Spin-1 Bosons*, Phys. Lett. B **703** (2011) 593, arXiv: `0908.0924 [hep-ph]`.

[53] D. M. Gingrich, *Quantum black holes with charge, colour, and spin at the LHC*, J. Phys. G **37** (2010) 105008, arXiv: `0912.0826 [hep-ph]`.

[54] X. Calmet, W. Gong and S. D. H. Hsu, *Colorful quantum black holes at the LHC*, Phys. Lett. B **668** (2008) 20, arXiv: `0806.4605 [hep-ph]`.

[55] D.-C. Dai et al., *BlackMax: a black-hole event generator with rotation, recoil, split branes, and brane tension*, Phys. Rev. D **77** (2008) 076007, arXiv: `0711.3012 [hep-ph]`.

[56] E. Eichten et al., *Supercollider physics*, Rev. Mod. Phys. **56** (1984) 579.

[57] E. Eichten et al., *Erratum: supercollider physics*, Rev. Mod. Phys. **58** (1986) 1065.

[58] P. Chiapetta and M. Perrottet, *Possible bounds on compositeness from inclusive one jet production in large hadron colliders*, Phys. Lett. B **253** (1991) 489.

[59] S. S. Wilks, *The large-sample distribution of the likelihood ratio for testing composite hypotheses*, Ann. Math. Statist. **9** (1938) 60.

[60] G. Choudalakis and D. Casadei, *Plotting the differences between data and expectation*, The European Physical Journal Plus **127** (2012) 1, ISSN: 2190-5444, URL: `http://dx.doi.org/10.1140/epjp/i2012-12025-y`.

[61] CDF Collaboration, T. Aaltonen et al., *Global search for new physics with 2.0 fb⁻¹ at CDF*, Phys. Rev. D **79** (2009) 011101, arXiv: `0809.3781 [hep-ex]`.

[62] G. Choudalakis, *On hypothesis testing, trials factor, hypertests and the BumpHunter*, 2011, arXiv: `1101.0390 [physics.data-an]`.

[63] H.-L. Lai et al., *New parton distributions for collider physics*, Phys. Rev. D **82** (2010) 074024, arXiv: `1007.2241 [hep-ph]`.

[64] A. D. Martin et al., *Parton distributions for the LHC*, Eur. Phys. J. C **63** (2009) 189, arXiv: `0901.0002 [hep-ph]`.

[65] A. L. Read, *Presentation of search results: the CL(s) technique*, J. Phys. G **28** (2002) 2693.

[66] T. Junk, *Confidence level computation for combining searches with small statistics*, Nucl. Instrum. Meth. A **434** (1999) 435, arXiv: `hep-ex/9902006 [hep-ex]`.

[67] S. B. Giddings and S. D. Thomas, *High-energy colliders as black hole factories: the end of short distance physics*, Phys. Rev. D **65** (2002) 056010, arXiv: `hep-ph/0106219 [hep-ph]`.

[68] S. Dimopoulos and G. L. Landsberg, *Black holes at the Large Hadron Collider*, Phys. Rev. Lett. **87** (2001) 161602, arXiv: `hep-ph/0106295 [hep-ph]`.

[69] P. Meade and L. Randall, *Black Holes and Quantum Gravity at the LHC*, JHEP **05** (2008) 003, arXiv: `0708.3017 [hep-ph]`.

[70] L. A. Anchordoqui et al., *Inelastic black hole production and large extra dimensions*, Phys. Lett. B **594** (2004) 363, arXiv: `hep-ph/0311365 [hep-ph]`.

[71] ATLAS Collaboration, *Search for strong gravity in multijet final states produced in pp collisions at $\sqrt{s}$ = 13 TeV using the ATLAS detector at the LHC*, JHEP **03** (2016) 026, arXiv: `1512.02586 [hep-ex]`.

[72] ATLAS Collaboration, *Search for TeV-scale gravity signatures in high-mass final states with leptons and jets with the ATLAS detector at $\sqrt{s}$ = 13 TeV*, (2016), submitted to Phys. Lett. B, arXiv: `1606.02265 [hep-ex]`.

[73] J. A. Frost et al., *Phenomenology of Production and Decay of Spinning Extra-Dimensional Black Holes at Hadron Colliders*, JHEP **10** (2009) 014, arXiv: `0904.0979 [hep-ph]`.

[74] N. Arkani-Hamed, S. Dimopoulos and G. R. Dvali, *The hierarchy problem and new dimensions at a millimeter*, Phys. Lett. B **429** (1998) 263, arXiv: `hep-ph/9803315 [hep-ph]`.

[75] I. Antoniadis et al., *New dimensions at a millimeter to a Fermi and superstrings at a TeV*, Phys. Lett. B **436** (1998) 257, arXiv: `hep-ph/9804398 [hep-ph]`.

[76] J. Pumplin et al., *New generation of parton distributions with uncertainties from global QCD analysis*, JHEP **07** (2002) 012, arXiv: `hep-ph/0201195 [hep-ph]`.

[77] J. Alwall et al., *The automated computation of tree-level and next-to-leading order differential cross sections, and their matching to parton shower simulations*, JHEP **07** (2014) 079, arXiv: `1405.0301 [hep-ph]`.

[78] M. V. Chizhov, *A Reference Model for Anomalously Interacting Bosons*, Phys. Part. Nucl. Lett. **8** (2011) 512, arXiv: `1005.4287 [hep-ph]`.

[79] ATLAS Collaboration, *Improved luminosity determination in pp collisions at $\sqrt{s}$ = 7 TeV using the ATLAS detector at the LHC*, Eur. Phys. J. C **73** (2013) 2518, arXiv: `1302.4393 [hep-ex]`.

[80] ATLAS Collaboration, *Luminosity determination in pp collisions at $\sqrt{s}$ = 8 TeV using the ATLAS detector at the LHC*, submitted to Eur. Phys. J. C (2016).

[81] J. Gao, *CIJET: a program for computation of jet cross sections induced by quark contact interactions at hadron colliders*, Comput. Phys. Commun. **184** (2013) 2362, arXiv: `1301.7263 [hep-ph]`.

[82] G. Cowan et al., *Asymptotic formulae for likelihood-based tests of new physics*, Eur. Phys. J. C **71** (2011) 1554, arXiv: `1007.1727 [physics.data-an]`.
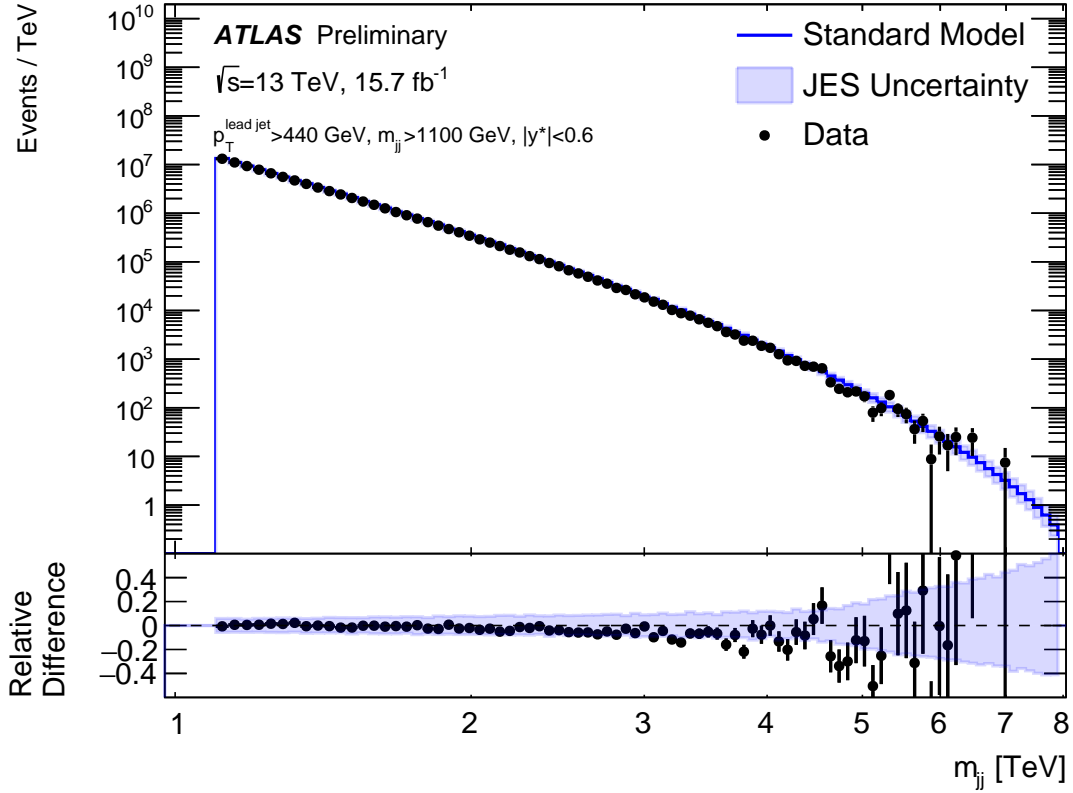
Appendix

Figure 7: The observed m_{jj} distribution obtained with the resonance analysis selection of events with $|y^*| < 0.6$ and $p_T > 440$ (60) GeV for the leading (subleading) jets. The distribution predicted by PYTHIA 8 simulation of QCD processes, corrected for NLO and EW effects, is overlaid. The shaded band indicates the experimental uncertainty on the jet energy scale calibration. Theoretical uncertainties are not depicted.
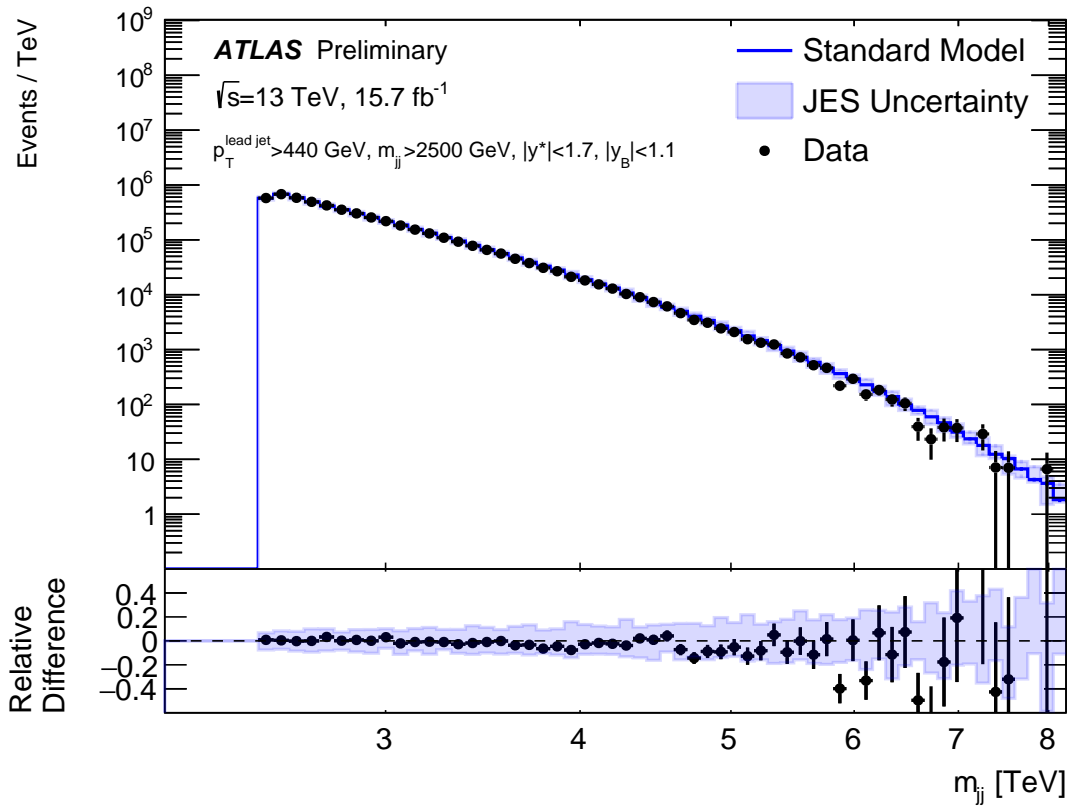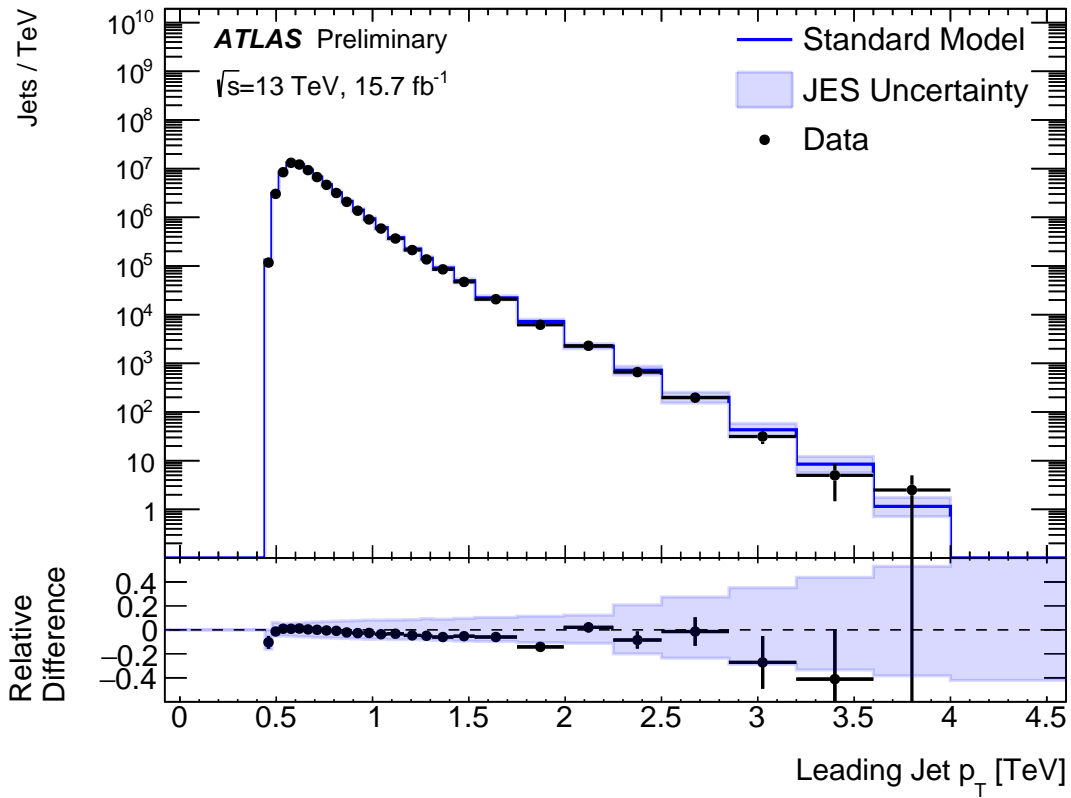
Figure 8: The observed m_{jj} distribution obtained in the angular analysis selection of events with $|y^*| < 1.7$, $|y_B| < 1.1$ and $p_T > 440$ (60) GeV for the leading (subleading) jets. The distribution predicted by PYTHIA 8 simulation of QCD processes, corrected for NLO and EW effects, is overlaid. The shaded band indicates the experimental uncertainty on the jet energy scale calibration. Theoretical uncertainties are not depicted.

Figure 9: The observed p_T distribution of the leading jet, obtained with the resonance analysis selection of events with $|y^*| < 0.6$ and $p_T > 60$ GeV for the subleading jet. The distribution predicted by Pythia 8 simulation of QCD processes, corrected for NLO and EW effects, is overlaid. The shaded band indicates the experimental uncertainty on the jet energy scale calibration. Theoretical uncertainties are not depicted.
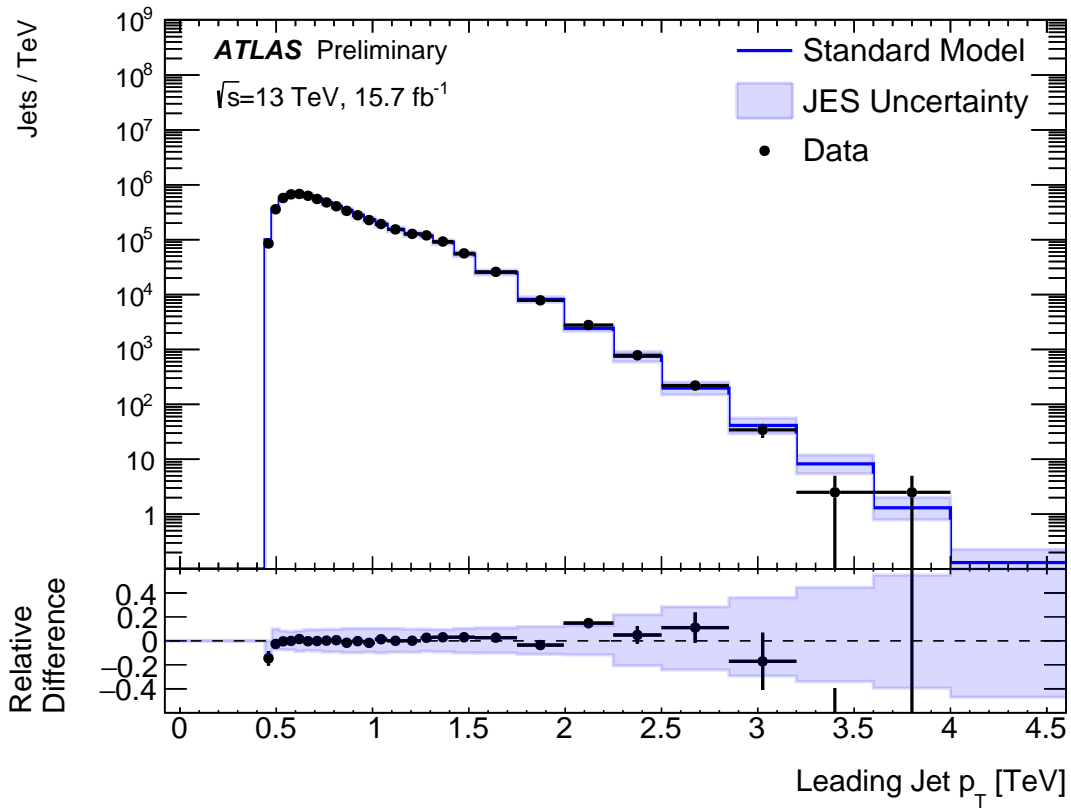
Figure 10: The observed p_T distribution of the leading jet, obtained with the angular analysis selection of events with $|y^*| < 1.7$, $|y_B| < 1.1$, and $p_T > 60$ GeV for the subleading jet. The distribution predicted by PYTHIA 8 simulation of QCD processes, corrected for NLO and EW effects, is overlaid. The shaded band indicates the experimental uncertainty on the jet energy scale calibration. Theoretical uncertainties are not depicted.
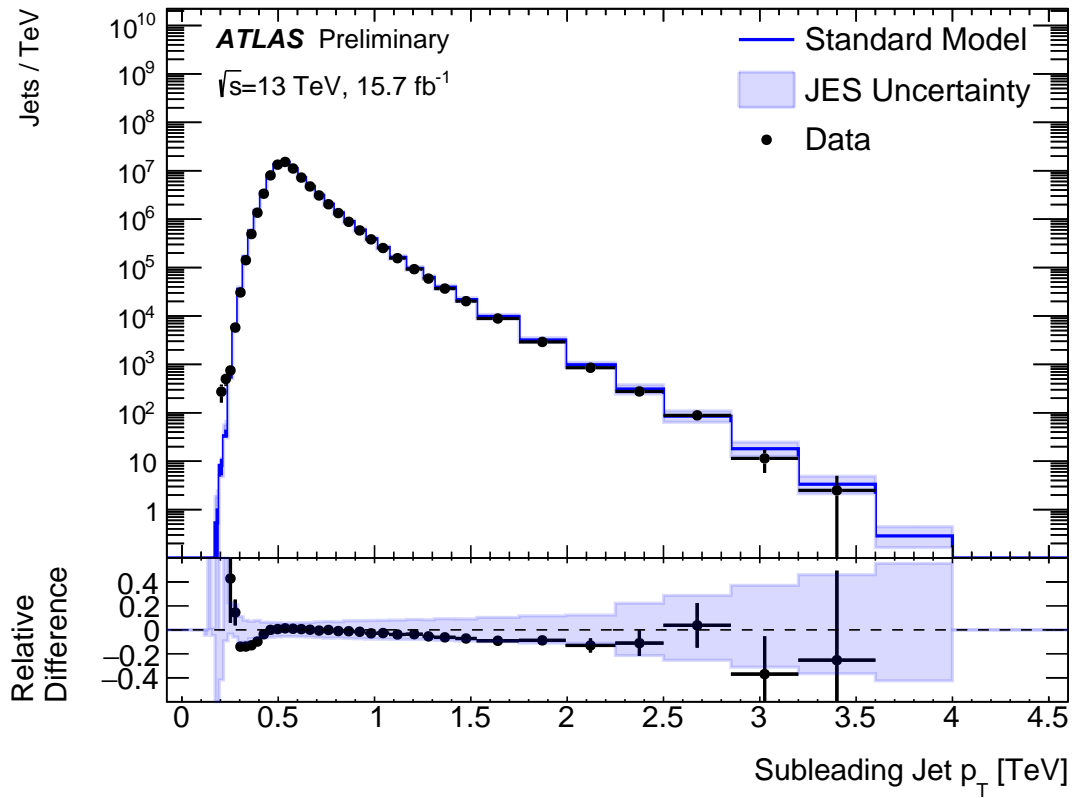
Figure 11: The observed p_T distribution of the subleading jet, obtained with the resonance analysis selection of events with $|y^*| < 0.6$ and $p_T > 440$ GeV for the leading jet. The distribution predicted by PYTHIA 8 simulation of QCD processes, corrected for NLO and EW effects, is overlaid. The shaded band indicates the experimental uncertainty on the jet energy scale calibration. Theoretical uncertainties are not depicted.
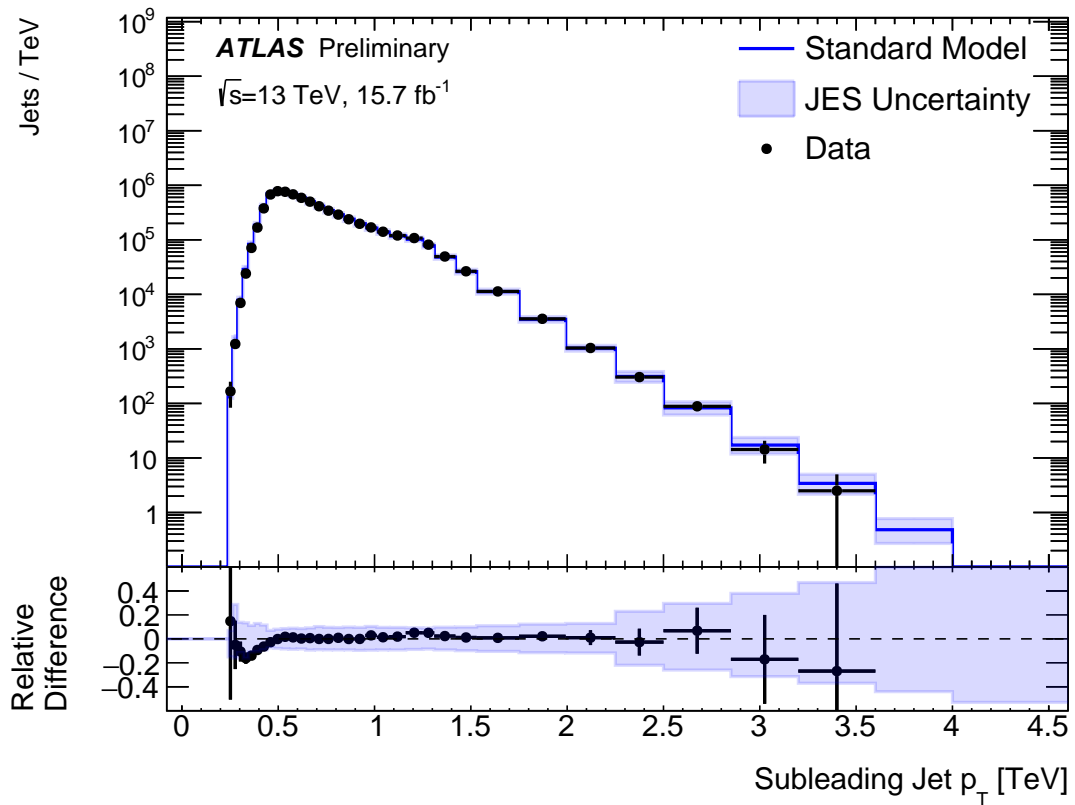
Figure 12: The observed p_T distribution of the subleading jet, obtained with the angular analysis selection of events with $|y^*| < 1.7$, $|y_B| < 1.1$, and $p_T > 440$ GeV for leading jet. The distribution predicted by PYTHIA 8 simulation of QCD processes, corrected for NLO and EW effects, is overlaid. The shaded band indicates the experimental uncertainty on the jet energy scale calibration. Theoretical uncertainties are not depicted.
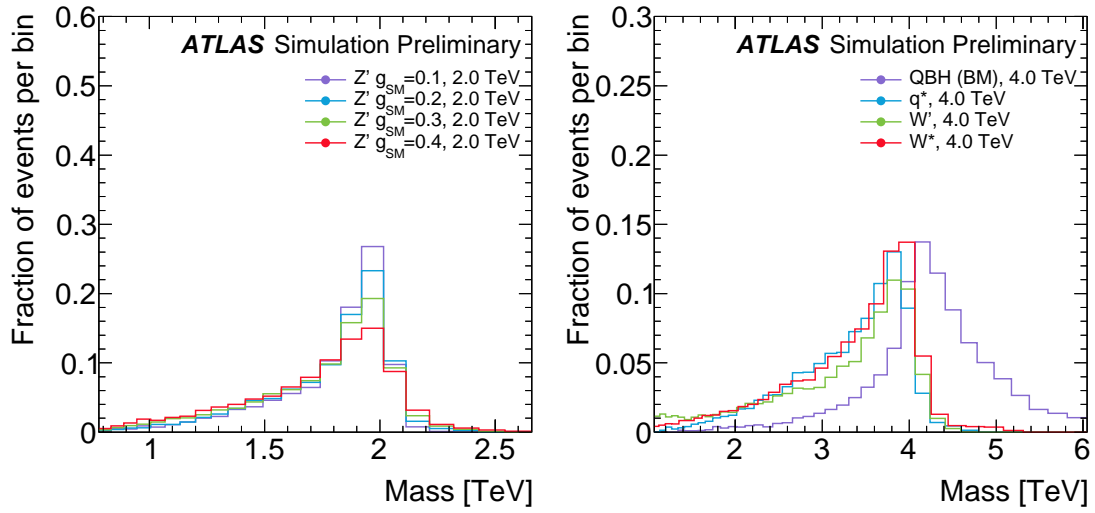
Figure 13: Comparison of a range of benchmark signal shapes after the resonant selection at a single common mass point. The W^* model uses the alternate selection with $y^* < 1.2$ while all other models use the nominal selection with $y^* < 0.6$. Z' samples are compared at a lower mass point than the remaining samples due to their restricted mass range.

(a) q^*

(b) BLACKMAX
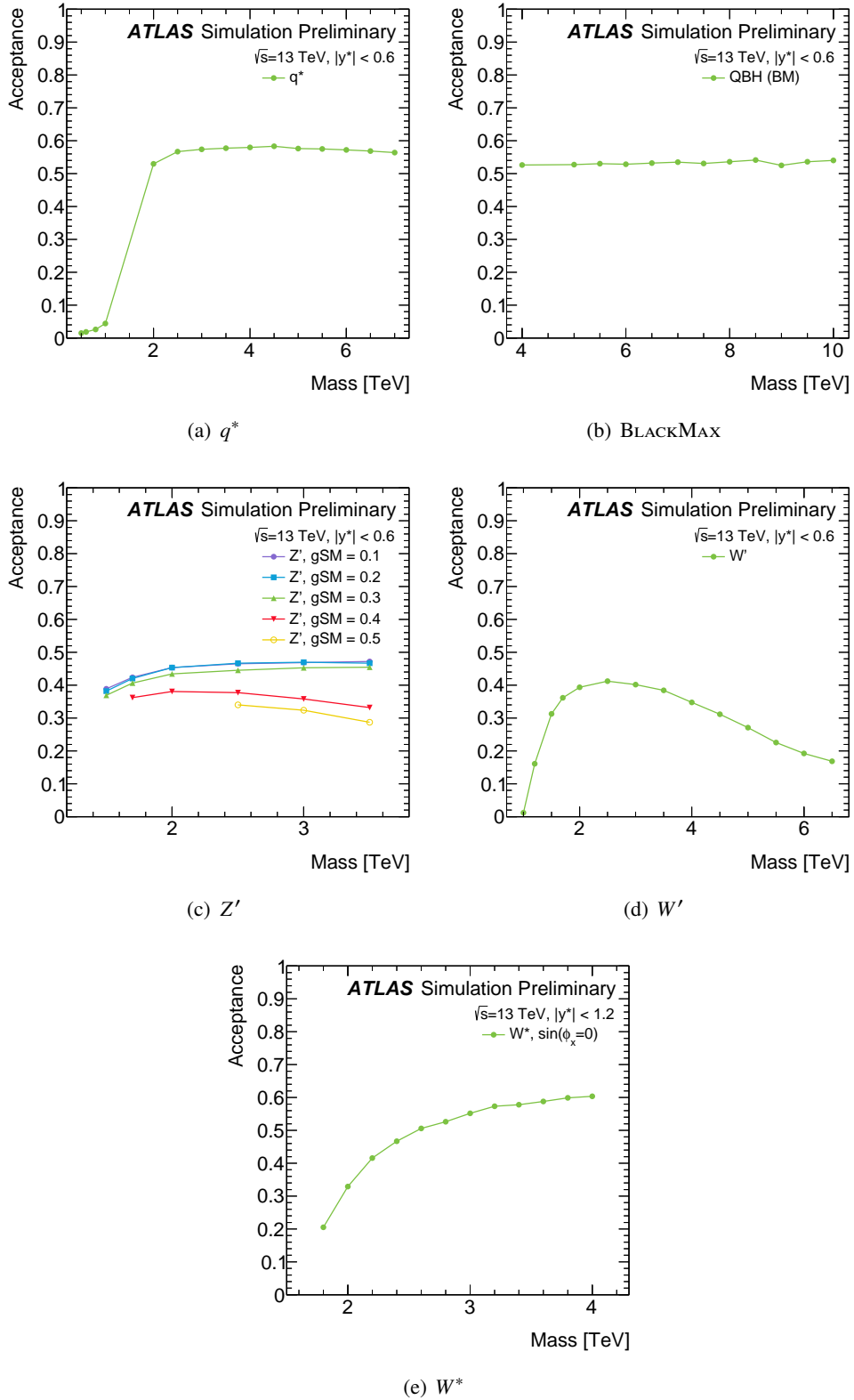
(c) Z'

(d) W'

(e) W^*

Figure 14: Acceptances versus mass for each resonant model, including cut on $m_{jj} > 1100$ GeV. The W^* model uses the alternate selection with $y^* < 1.2$ while all other models use the nominal selection with $y^* < 0.6$.
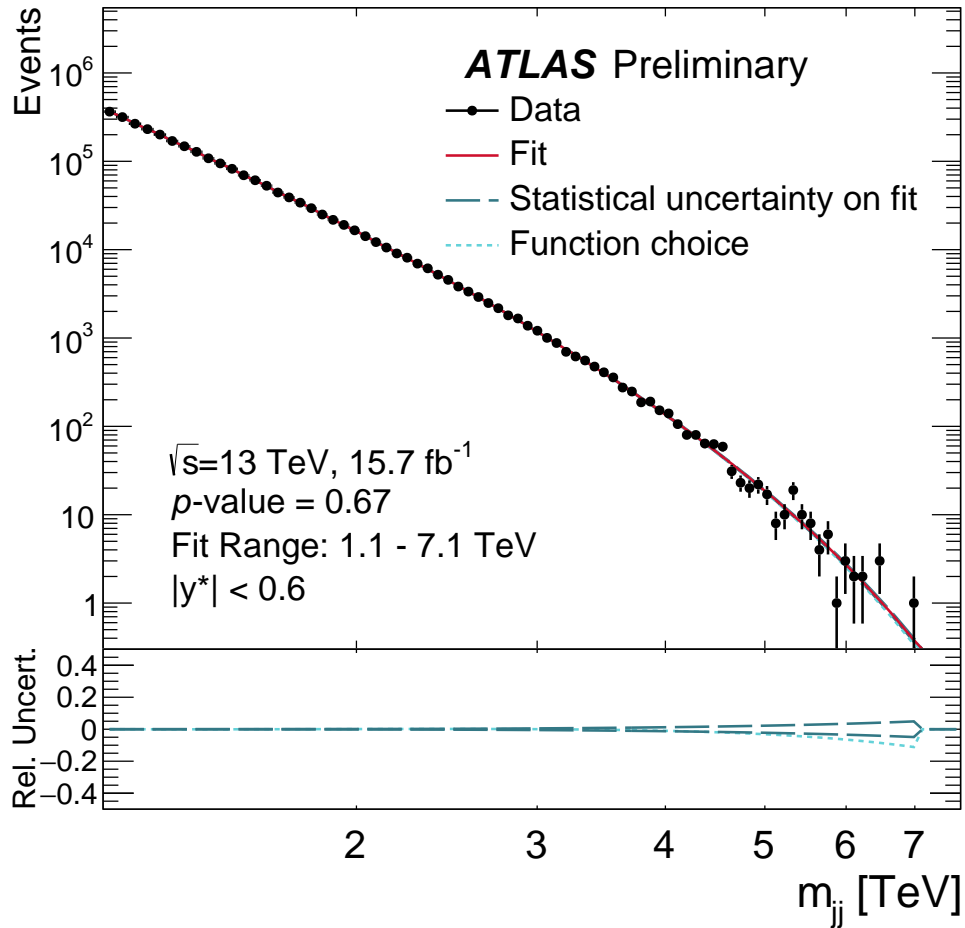
Figure 15: The fit to the m_{jj} distribution with $|y^*| < 0.6$ (red) with its two uncertainties. The dark blue line with long dashes indicates the statistical uncertainty on the fit, corresponding to the variability in the fit results across a large collection of pseudoexperiments. The light blue line with short dashes indicates the uncertainty on the function choice, based on comparison to a function with a higher number of parameters.
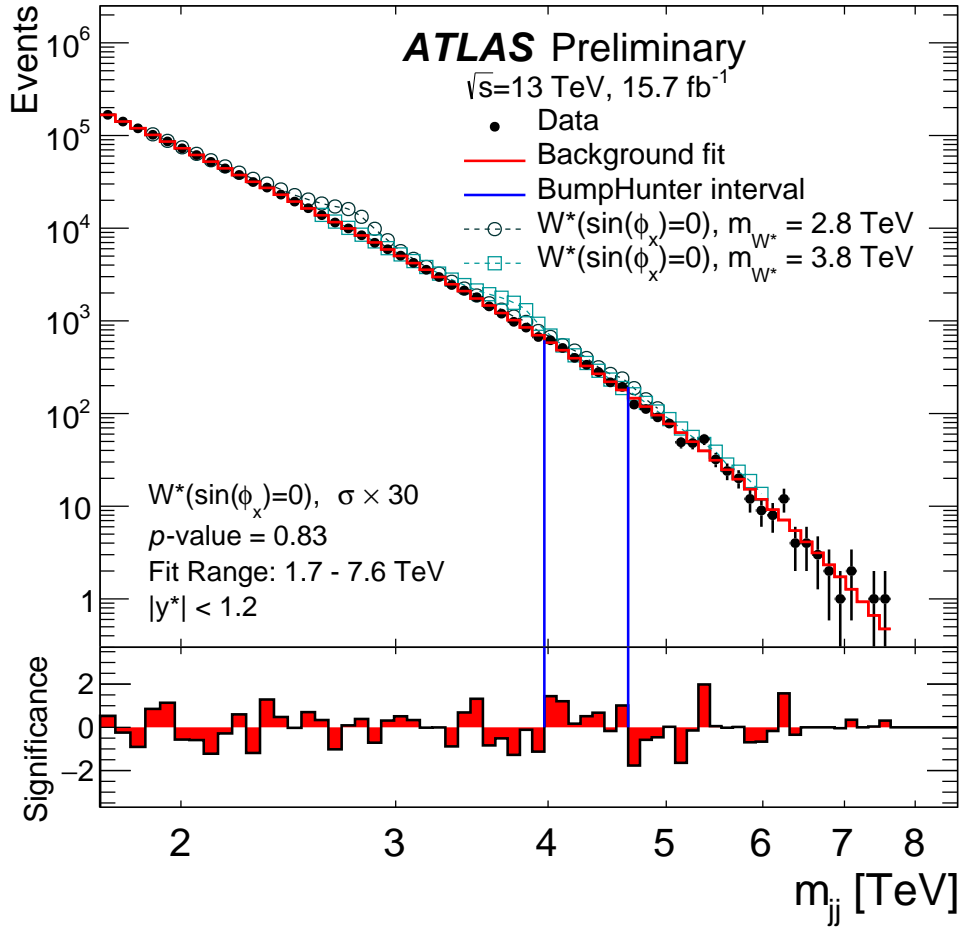
Figure 16: The reconstructed dijet mass distribution (filled points) for events with $|y^*| < 1.2$ and $p_T > 440\,(60)$ GeV for the leading (subleading) jets. The solid line depicts the fit to Eq. (1), as discussed in the text. Predictions for a chiral W boson are shown above the fit, normalized to 30 times the predicted cross-section in order to make the shapes distinguishable above the data. The vertical lines indicate the most discrepant interval identified by the BumpHunter algorithm, for which the p-value is stated in the figure. The lower panel shows the bin-by-bin significances of the data–fit differences, considering only statistical uncertainties.

Figure 17: The reconstructed dijet mass distribution (filled points) for events with $|y^*| < 0.6$ and $p_T > 440\,(60)$ GeV for the leading (subleading) jets. The solid line depicts the fit to Eq. (1), as discussed in the text. Predictions for the W' signal for two masses are shown above the fit, normalized to the predicted cross-section, scaled up by a factor 100 for visibility. The vertical lines indicate the most discrepant interval identified by the BumpHunter algorithm, for which the p-value is stated in the figure. The lower panel shows the bin-by-bin significances of the data–fit differences, considering only statistical uncertainties.
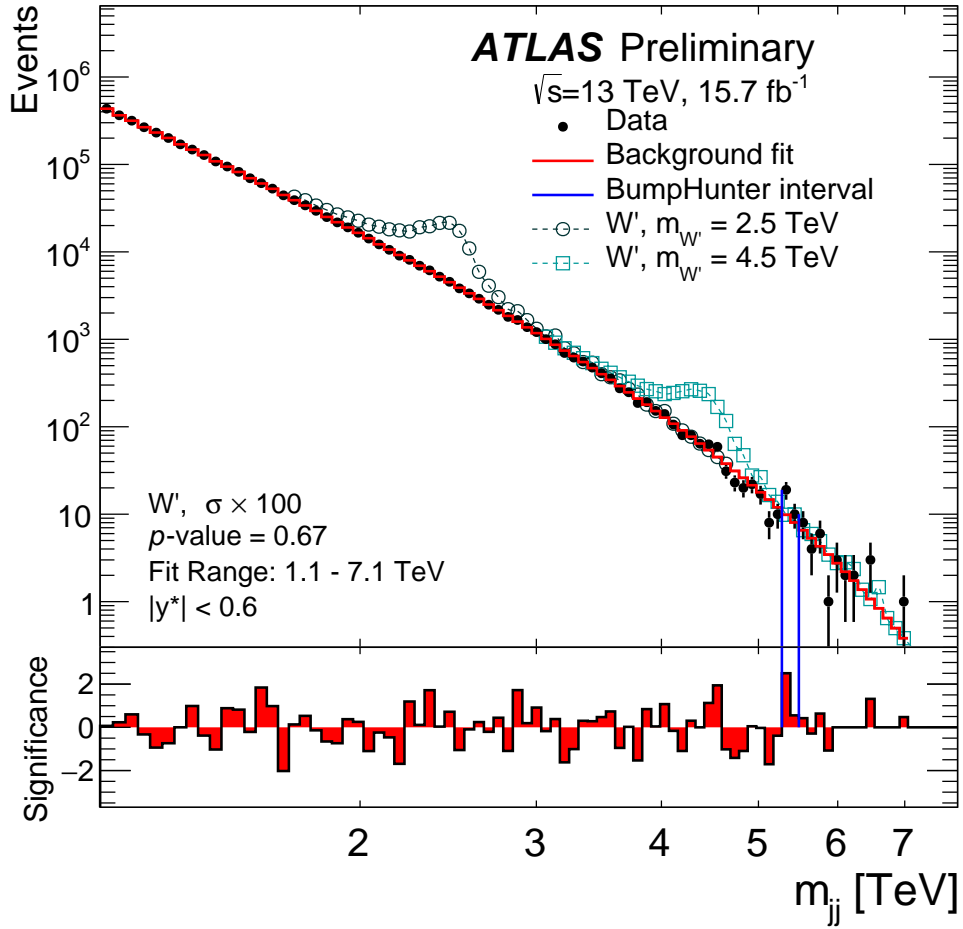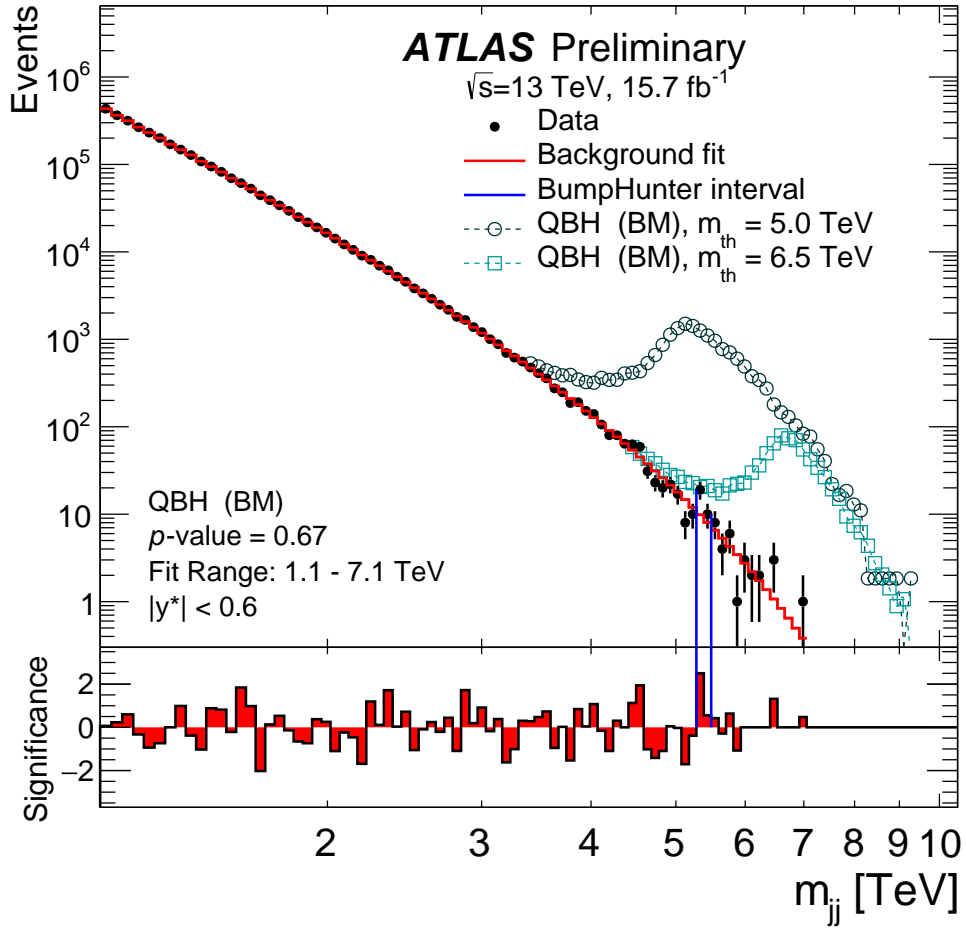
Figure 18: The reconstructed dijet mass distribution (filled points) for events with $|y^*| < 0.6$ and $p_T > 440\,(60)$ GeV for the leading (subleading) jets. The solid line depicts the fit to Eq. (1), as discussed in the text. Predictions from BLACKMAX with n=6 for two threshold masses are shown above the fit, normalized to the predicted cross-section. The vertical lines indicate the most discrepant interval identified by the BUMPHUNTER algorithm, for which the p-value is stated in the figure. The lower panel shows the bin-by-bin significances of the data–fit differences, considering only statistical uncertainties.

Figure 19: The highest-mass, central dijet event passing the dijet resonance selection (Event 2504627221, Run 302053): the two central high-p_T jets have transverse momenta of 2.93 and 2.77 TeV, they have a $|y^*|$ of 0.51 and their invariant mass is 6.46 TeV.

Figure 20: The highest-mass dijet event passing the angular selection (Event 753275626, Run 302347): the two central high-p_{T} jets have transverse momenta of 3.13 and 2.98 TeV, they have a $|y^*|$ of 0.66 and their invariant mass is 7.5 TeV.
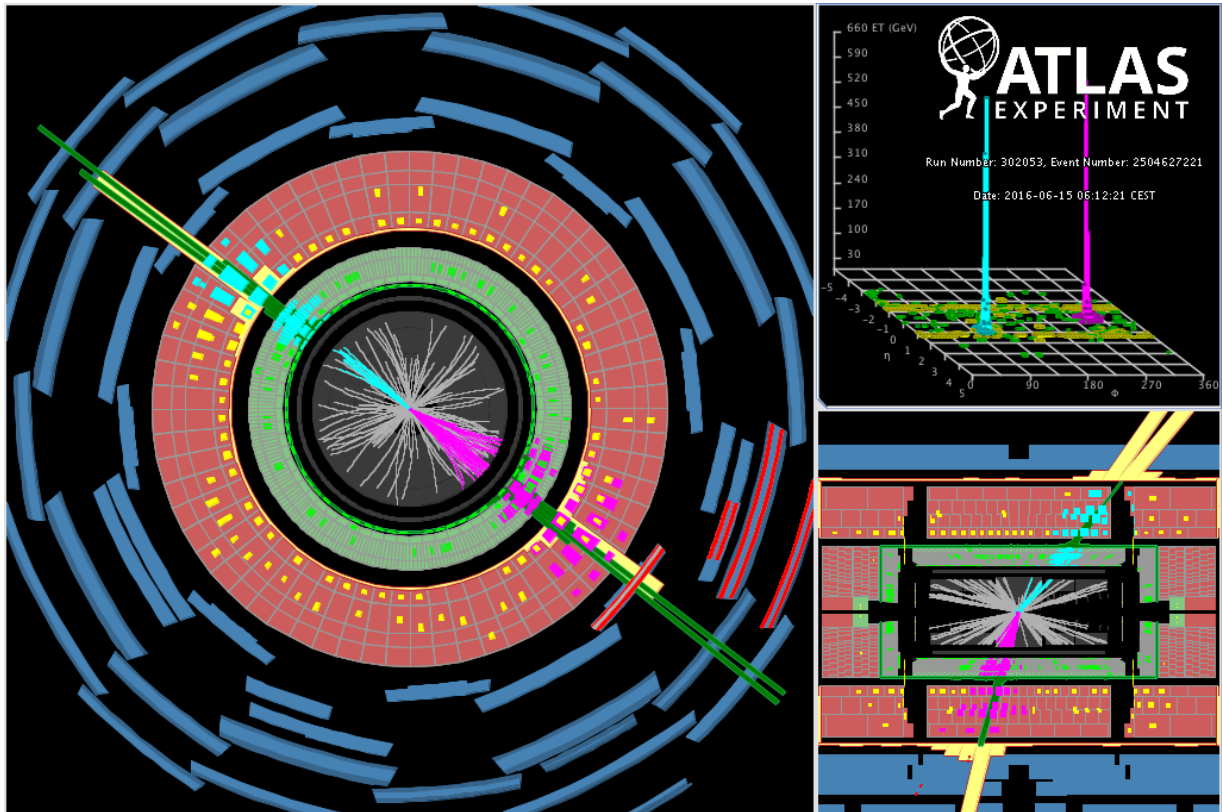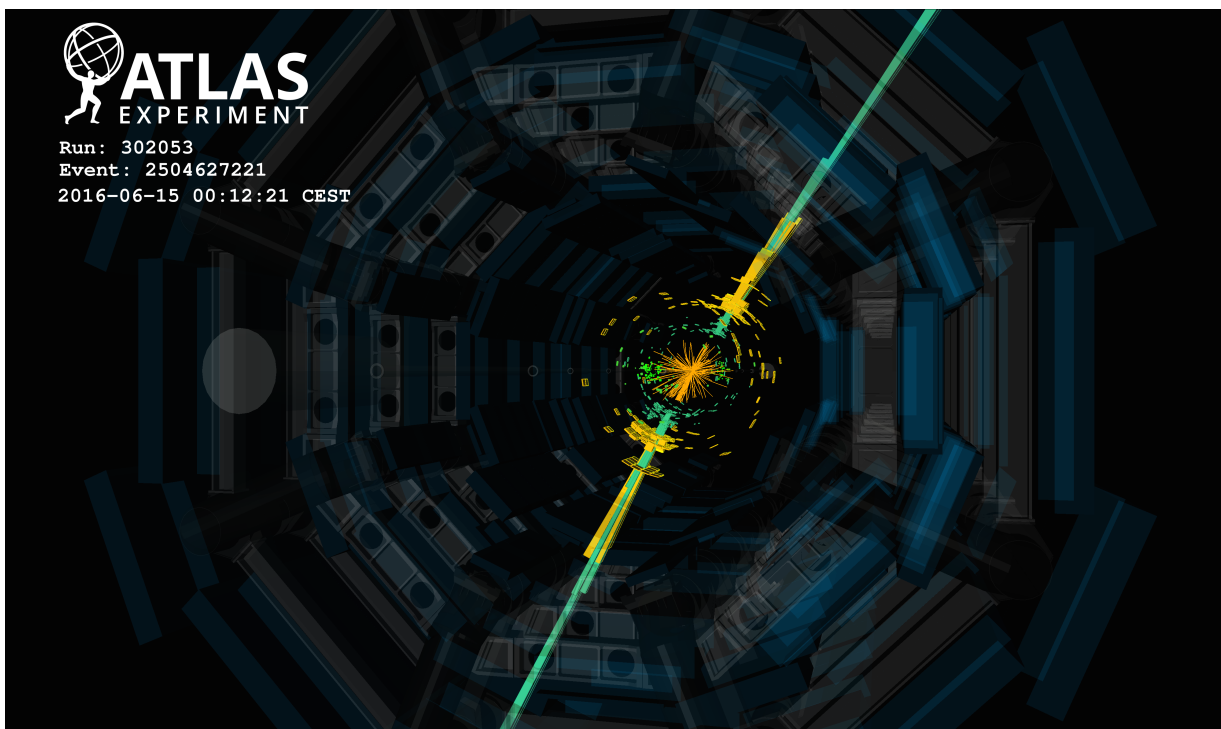
Figure 21: The highest-mass, central dijet event passing the dijet resonance selection (Event 2504627221, Run 302053): the two central high-p_T jets have transverse momenta of 2.93 and 2.77 TeV, they have a $|y^*|$ of 0.51 and their invariant mass is 6.46 TeV.
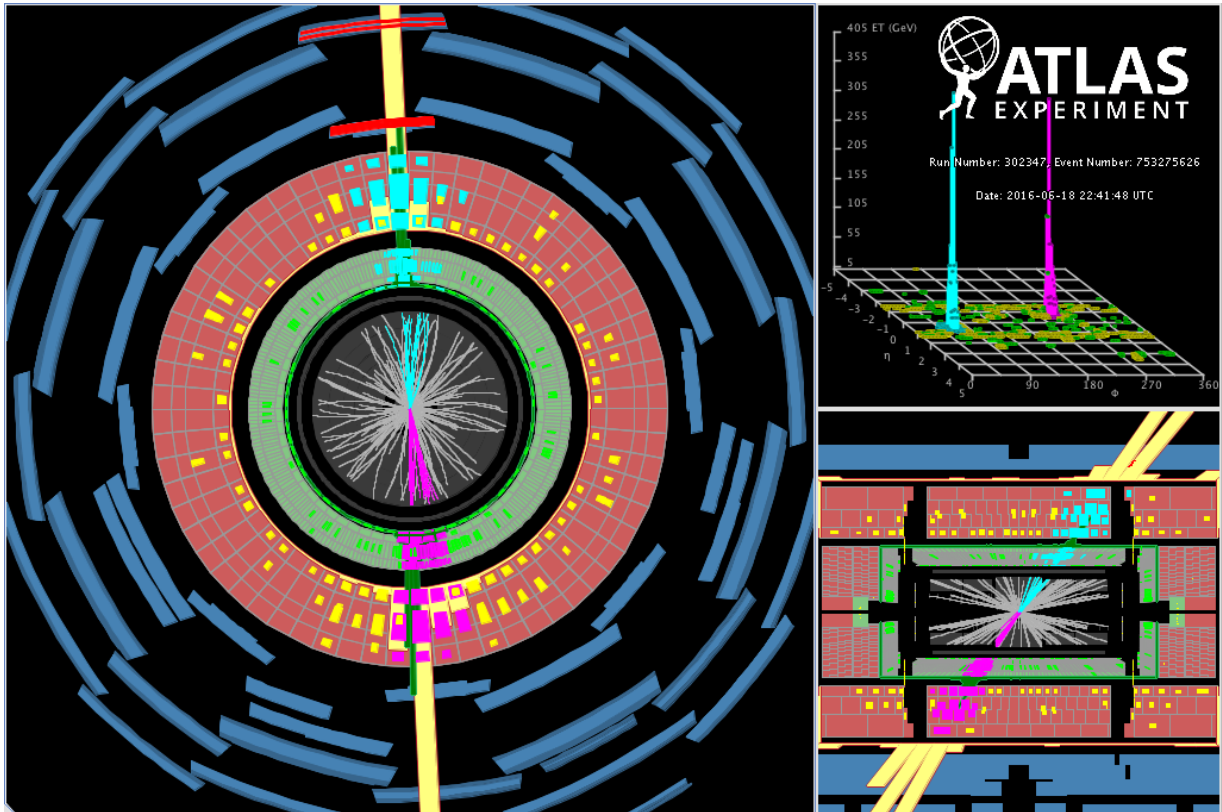
Figure 22: The highest-mass dijet event passing the angular selection (Event 753275626, Run 302347): the two central high-p_T jets have transverse momenta of 3.13 and 2.98 TeV, they have a $|y^*|$ of 0.66 and their invariant mass is 7.5 TeV.
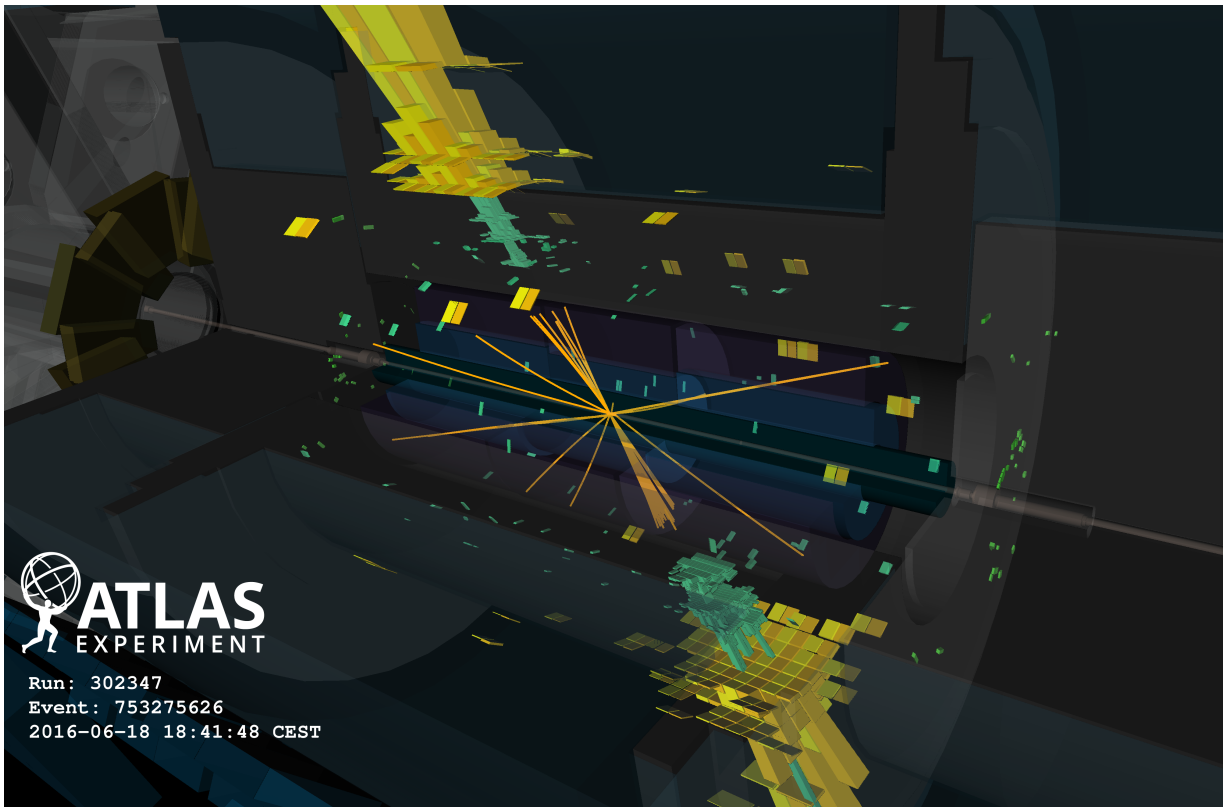
m_G [TeV]	Observed 95% CL upper limits on $\sigma \times \mathcal{A} \times BR$ [fb]			
	σ_G/m_G =Res.	$\sigma_G/m_G = 7\%$	$\sigma_G/m_G = 10\%$	$\sigma_G/m_G = 15\%$
1.2	145.0	-	-	-
1.25	87.3	189.0	-	-
1.3	97.4	168.0	246.0	-
1.35	118.0	177.0	284.0	607.0
1.4	86.9	196.0	353.0	574.0
1.45	89.4	236.0	358.0	504.0
1.5	110.0	244.0	334.0	360.0
1.55	114.0	222.0	265.0	249.0
1.6	114.0	171.0	196.0	162.0
1.65	78.1	122.0	133.0	135.0
1.7	42.0	87.0	101.0	111.0
1.75	44.8	70.1	83.1	92.0
1.8	40.7	59.4	68.1	84.1
1.85	31.6	49.5	60.2	75.9
1.9	29.4	44.0	53.0	69.5
1.95	30.3	39.9	47.3	66.4
2.0	27.5	35.6	46.0	63.3
2.1	18.2	34.2	45.0	57.2
2.2	20.7	38.5	44.3	73.7
2.3	33.5	48.0	54.6	66.9
2.4	29.4	42.2	49.7	63.8
2.5	14.5	33.4	45.1	56.5
2.6	12.5	28.9	39.0	46.9
2.7	12.0	27.4	34.6	38.0
2.8	11.8	25.5	28.8	28.9
2.9	14.6	22.0	22.1	24.3
3.0	12.5	16.2	18.0	20.4
3.1	8.55	12.9	15.4	18.5
3.2	4.82	10.9	13.4	16.6
3.3	5.21	9.69	11.9	15.2
3.4	6.5	9.11	10.6	13.9
3.5	6.48	8.25	10.2	12.6
3.6	5.05	7.6	9.31	11.2
3.7	3.29	7.06	8.63	10.1
3.8	3.27	6.61	8.28	9.12
3.9	3.98	6.38	7.8	8.28
4.0	4.01	6.05	7.11	7.27
4.2	2.33	5.31	5.34	5.86
4.4	3.29	3.94	4.08	4.58
4.6	3.11	2.7	3.25	3.86
4.8	1.46	2.06	2.74	3.13
5.0	1.01	1.94	2.4	2.58
5.2	1.53	1.92	2.14	2.17
5.4	1.65	1.77	1.79	1.79
5.6	1.6	1.53	1.5	1.49
5.8	1.25	1.22	1.17	1.29
6.0	0.538	0.956	1.0	1.18
6.2	0.482	0.74	0.88	-
6.4	0.469	0.658	0.789	-
6.6	0.443	-	-	-

Table 2: Observed limit on $\sigma \times \mathcal{A} \times BR$ for each width and mass of Gaussian signal shape tested.

Mass Bins (TeV)								
1.100	–	1.133	2.542	–	2.600	5.074	–	5.175
1.133	–	1.166	2.600	–	2.659	5.175	–	5.277
1.166	–	1.200	2.659	–	2.719	5.277	–	5.381
1.200	–	1.234	2.719	–	2.780	5.381	–	5.487
1.234	–	1.269	2.780	–	2.842	5.487	–	5.595
1.269	–	1.305	2.842	–	2.905	5.595	–	5.705
1.305	–	1.341	2.905	–	2.969	5.705	–	5.817
1.341	–	1.378	2.969	–	3.034	5.817	–	5.931
1.378	–	1.416	3.034	–	3.100	5.931	–	6.047
1.416	–	1.454	3.100	–	3.167	6.047	–	6.165
1.454	–	1.493	3.167	–	3.235	6.165	–	6.285
1.493	–	1.533	3.235	–	3.305	6.285	–	6.407
1.533	–	1.573	3.305	–	3.376	6.407	–	6.531
1.573	–	1.614	3.376	–	3.448	6.531	–	6.658
1.614	–	1.656	3.448	–	3.521	6.658	–	6.787
1.656	–	1.698	3.521	–	3.596	6.787	–	6.918
1.698	–	1.741	3.596	–	3.672	6.918	–	7.052
1.741	–	1.785	3.672	–	3.749	7.052	–	7.188
1.785	–	1.830	3.749	–	3.827	7.188	–	7.326
1.830	–	1.875	3.827	–	3.907	7.326	–	7.467
1.875	–	1.921	3.907	–	3.988	7.467	–	7.610
1.921	–	1.968	3.988	–	4.070	7.610	–	7.756
1.968	–	2.016	4.070	–	4.154	7.756	–	7.904
2.016	–	2.065	4.154	–	4.239	7.904	–	8.055
2.065	–	2.114	4.239	–	4.326	8.055	–	8.208
2.114	–	2.164	4.326	–	4.414	8.208	–	8.364
2.164	–	2.215	4.414	–	4.504	8.364	–	8.523
2.215	–	2.267	4.504	–	4.595	8.523	–	8.685
2.267	–	2.320	4.595	–	4.688	8.685	–	8.850
2.320	–	2.374	4.688	–	4.782	8.850	–	9.019
2.374	–	2.429	4.782	–	4.878	9.019	–	9.191
2.429	–	2.485	4.878	–	4.975	9.191	–	9.366
2.485	–	2.542	4.975	–	5.074	9.366	–	9.544

Table 3: Bin edges used for the binned dijet mass distribution in Fig. 1 and the statistical analysis of resonant signals.